JℲM PAPERS

Modelling the effect of roughness density on turbulent forced convection

W. Abu Rowin[1],†, K. Zhong[1], T. Saurav[1], T. Jelly[1], N. Hutchins[1] and D. Chung[1]

[1]Department of Mechanical Engineering, University of Melbourne, Victoria 3010, Australia

By examining a systematic set of direct numerical simulations, we develop a model which captures the effect of roughness density on global and local heat transfer in forced convection. The surfaces considered are zero-skewed three-dimensional sinusoidal rough walls with solidities, Λ (defined as the frontal area divided by the total plan area), ranging from low $\Lambda = 0.09$, medium $\Lambda = 0.18$ to high $\Lambda = 0.36$. For each solidity, we vary the roughness height characterised by the roughness Reynolds number, k^+, from transitionally rough to fully rough conditions. The findings indicate that, as the fully rough regime is approached, there is a pronounced breakdown in the analogy between heat and momentum transfer, whereby the velocity roughness function ΔU^+ continues to increase and the temperature roughness function $\Delta \Theta^+$ attains a peak with increasing k^+. This breakdown occurs at higher sand-grain roughness Reynolds numbers (k_s^+) with increasing solidity. Locally, we find that the heat transfer can be meaningfully partitioned into two categories: exposed, high-shear regions experiencing higher heat transfer obeying a local Reynolds analogy and sheltered, reversed-flow regions experiencing lower and spatially uniform heat transfer. The relative contribution of these distinct mechanisms to the global heat transfer depends on the fraction of the total surface area covered by these regions, which ultimately depends on Λ. These insights enable us to develop a model for the rough-wall heat-transfer coefficient, $C_{h,k}(k^+, \Lambda, Pr)$, where Pr is the molecular Prandtl number, that assumes different heat-transfer laws in exposed and sheltered regions. We show that the exposed–sheltered surface-area fractions can be modelled through simple ray tracing that is solely dependent on the surface topography and a prescribed sheltering angle. Model predictions compare well when applied to heat-transfer data of traverse ribs from the literature.

Key words: turbulent convection, turbulence simulation, turbulent boundary layers

† Email address for correspondence: aburowin@ualberta.ca

1. Introduction

Turbulent flow over rough walls has been an area of intense research owing to its ubiquity in a wide range of engineering and naturally occurring systems. Despite this interest, the effects of rough walls on momentum and heat transfer are far less understood than their smooth-wall counterparts (Jiménez 2004; Kays, Crawford & Weigand 2005; Chung *et al.* 2021). This lack of understanding, particularly for heat transfer, is attributed to the difficulty associated with obtaining systematic, detailed flow data for rough-wall flows. Understanding the relationship between turbulence, surface roughness and heat transfer is crucial for maximising operational efficiency in applications like heat exchangers and turbines.

Surface roughness exhibits a wide range of diverse topographical forms (Ligrani, Oliveira & Blaskovich 2003; Chung *et al.* 2021). The objective is to understand and predict the influence of these topographical features on drag and heat transfer. To accomplish this, the discipline has endeavoured to classify surfaces based on attributes such as roughness height, density and distribution, all of which have been demonstrated to impact fluid flow (Raupach, Antonia & Rajagopalan 1991; Flack & Schultz 2010; Chung *et al.* 2021). Several different measures for roughness height have been used, such as the average roughness height, k_a (the mean of the absolute roughness fluctuation relative to the mean elevation), the peak-to-trough height, k_p, and the root-mean-square height, k_{rms} (Chung *et al.* 2021). Different measures are also introduced for the roughness density, including the ratio of the frontal projected area of roughness elements in the flow direction to the total plan area, known as the frontal solidity, Λ. The frontal solidity is also defined as half of the mean absolute streamwise gradient of the roughness elevation, known as the effective slope, *ES*. Related to density and roughness distribution, the plan solidity, Λ_p, is defined as the ratio of the plan area of roughness elements to the total plan area. The roughness distribution is also often described by the skewness, *Sk*, which is the roughness vertical asymmetry, showing whether the roughness primarily comprises peaks ($Sk > 0$) or valleys ($Sk < 0$). Skewness is closely related to plan solidity (Chung *et al.* 2021). By selecting the appropriate roughness parameters, it is possible to develop useful empirical correlations between the topographical characteristics of a surface and its effect on momentum and heat transfer.

The effect of roughness on the mean flow and turbulence has been vigorously studied (e.g. the early pioneering studies Nikuradse 1933; Colebrook & White 1937; Perry & Joubert 1963). It is well established that surface roughness increases drag and thus shifts the logarithmic region of the mean streamwise velocity profile downward by the roughness function, ΔU^+, (Clauser 1954; Hama 1954) when compared with that of the smooth wall

$$U^+ = \frac{1}{\kappa} \log(z^+ - d^+) + A - \Delta U^+. \tag{1.1}$$

Here, ΔU^+ is subtracted from the log law of a smooth-wall turbulent flow, where U is the mean streamwise velocity, $\kappa \approx 0.4$ is the von Kármán constant, z is the wall-normal distance, d is a virtual-origin shift defined more formally in § 3.1 and $A \approx 5.0$ is the log intercept for the smooth wall. The superscript '+' denotes parameters normalised with inner variables (i.e. friction velocity, $U_\tau \equiv (\langle \tau_w \rangle / \rho)^{1/2}$, and kinematic viscosity, ν, where $\langle \tau_w \rangle$ is the total wall shear stress encompassing pressure and viscous drag per unit plan area and ρ is the fluid density). Rough-wall drag must be determined based on topographical properties and the viscous length scale ν / U_τ. The logarithmic shift is zero ($\Delta U^+ = 0$) when the wall is aerodynamically smooth (i.e. the roughness height is small relative to the wall unit ν / U_τ). With increasing viscous-scaled roughness height, a shift is observed

$(\Delta U^+ > 0)$ for the transitionally rough regime. Ultimately, in the fully rough regime, when the roughness height is much larger than ν/U_τ, this shift is given by

$$\Delta U^+ = \frac{1}{\kappa} \log(k_s^+) + A - C_N. \tag{1.2}$$

Here, k_s is the equivalent close-packed uniform sand-grain roughness as proposed by Schlichting (1936) and $C_N \approx 8.5$ is Nikuradse's fully rough constant for such surfaces (Nikuradse 1933). Several experimental and numerical studies have shown for matched k^+ that ΔU^+ depends on the roughness density (Dirling 1973; Simpson 1973; Macdonald, Griffiths & Hall 1998; Waigh & Kind 1998; van Rij, Belnap & Ligrani 2002; Chan *et al.* 2015; Leonardi *et al.* 2015; Placidi & Ganapathisubramani 2015; MacDonald *et al.* 2016; Forooghi *et al.* 2018c; Yang *et al.* 2022). In general, for fixed k^+, these studies found a trend of increasing ΔU^+ with increasing Λ within the sparse regime where $\Lambda \lesssim 0.15$. For further increases of $\Lambda \gtrsim 0.15$ towards the dense regime, a reduction of ΔU^+ was observed. Care should be taken in interpreting these results, since some studies that reported this trend also varied skewness (Leonardi *et al.* 2015; Forooghi *et al.* 2018c). When the skewness is fixed in the fully rough regime, the transition from sparse to dense regimes was reported at greater solidities of $\Lambda = 0.21$ for block roughness (Placidi & Ganapathisubramani 2015). When irregular roughness is introduced, a monotonic increase of ΔU^+ with increasing Λ is observed in the fully rough regime. Examples include roughness over hydraulic turbine blades (Yuan & Piomelli 2014) and irregular rough surfaces (Kuwata & Nagura 2020; Kuwata 2021).

These different observations suggest that the transition from sparse to dense roughness spacing may also depend on the skewness (Sk), roughness regime (transitional or fully rough) and roughness regularity. Thus, in order to better understand the effects of the solidity on drag systematically, the present study will consider constant $Sk = 0$ surfaces while varying k^+ to sweep though transitionally and fully rough conditions for a regular three-dimensional sinusoidal roughness of varying solidity.

Surface roughness has a comparable effect on the mean temperature to that on the mean streamwise velocity when $k_s^+ \lesssim 100$ (Owen & Thomson 1963; Yaglom & Kader 1974). The higher roughness size shifts the mean logarithmic temperature profile downward by the temperature roughness function, $\Delta \Theta^+$ (Yaglom 1979). Here, the superscript '+' for temperature denotes normalisation with the friction temperature, $\Theta_\tau \equiv \langle q_w \rangle/(\rho c_p U_\tau)$, where $\langle q_w \rangle$ is the wall heat transfer per unit plan area (i.e. heat flux) and c_p is the specific heat at constant pressure. Thus, the rough-wall logarithmic temperature profile is (Dipprey & Sabersky 1963; Owen & Thomson 1963; Yaglom 1979)

$$\Theta^+ = \frac{1}{\kappa_h} \log(z^+ - d^+) + A_h - \Delta \Theta^+ \tag{1.3a}$$

$$= \frac{1}{\kappa_h} \log\left(\frac{z - d}{k_s}\right) + g. \tag{1.3b}$$

Here, $\Theta^+ \equiv (\Theta - \Theta_w)/\Theta_\tau$, where Θ is the mean fluid temperature which is a function of wall-normal distance $\Theta(z)$, Θ_w is the wall temperature, $\kappa_h \approx \kappa/Pr_t \approx 0.47$ is the logarithmic temperature profile slope, $Pr_t \approx 0.85$ is the turbulent Prandtl number, assumed constant in the logarithmic region (Alcántara-Ávila, Hoyas & Pérez-Quiles 2021), and $A_h(Pr)$ is the smooth-wall log intercept which depends on the Prandtl number $Pr \equiv \nu/\alpha$, where α is the thermal diffusivity (Kader 1981; Pirozzoli 2023). Equation (1.3b) provides a common alternative formulation adopting the so-called *g*-function, which

979 A22-3

	Roughness geometry	k_s^+-range	$g(k_s^+, Pr)$
Dipprey & Sabersky (1963)	Sand grains	$k_s^+ \gtrsim 65$	$5.19(k_s^+)^{0.20}Pr^{0.44}$
Owen & Thomson (1963)	Irregular	$k_s^+ \gtrsim 70$	$0.52(k_s^+)^{0.45}Pr^{0.80}$
Sheriff & Gumley (1966)	Spanwise rods	$k_s^+ \gtrsim 50$	$5.37(k_s^+)^{0.20} + 2.03$
Webb, Eckert & Goldstein (1971)	Spanwise ribs	$k_s^+ \gtrsim 25$	$4.50(k/k_s)^{0.28}(k_s^+)^{0.28}Pr^{0.57}$ $-(1/\kappa_h)\log(k_s/k),$ $k_s/k = \exp[\kappa(8.5 - 0.95\Lambda^{-0.53})]$
Yaglom & Kader (1974)	Regular[a]	$k_s^+ \gtrsim 70$	$0.55(k_s^+)^{1/2}(Pr^{2/3} - 0.2) + 9.5$
Brutsaert (1975)	—	$k_s^+ \gtrsim 60$	$3.12(k_s^+)^{1/4}Pr^{1/2} + 3.5$

Table 1. Proposals for the *g*-function scaling in (1.4).

[a]Yaglom & Kader (1974) validated their expression with roughness arrangements of close-packed spheres, cylinders and the wave-form roughness elements of Chamberlain (1968).

may be interpreted as an (inverse) rough-wall heat-transfer coefficient (Stanton number), $g^{-1} \equiv \langle q_w \rangle / (\rho c_p U_\tau \Theta_{k_s}) \equiv 1/\Theta_{k_s}^+$, where $\Theta_{k_s} \equiv \Theta(z - d = k_s)$ (Dipprey & Sabersky 1963; Owen & Thomson 1963; Webb *et al.* 1971). Fully rough heat-transfer prediction typically takes the form of a power-law scaling for the *g*-function

$$g \sim (k_s^+)^p Pr^m, \tag{1.4}$$

where *p* and *m* are model exponents to be determined. Table 1 documents some of the diverse proposals for (1.4) in the literature. Although most predictions for these exponents are empirical, noteworthy are the theory-based predictions of Brutsaert (1975), $g \sim (k_s^+)^{1/4}Pr^{1/2}$, and Yaglom & Kader (1974), $g \sim (k_s^+)^{1/2}Pr^{2/3}$. The correct values to take for these exponents have remained a topic of debate in the literature (Li *et al.* 2017, 2020; Zhong, Hutchins & Chung 2023). Notably, however, we highlight how an understanding of the dependency of *g* with respect to Λ, i.e. $g(k_s^+, Pr, \Lambda)$ is currently lacking (table 1), except for the formulation of Webb *et al.* (1971). In figure 1, we showcase our present direct numerical simulation (DNS) data at varying (k_s^+, Λ) alongside the experimental data of Webb *et al.* (1971). Here, a clear sensitivity of *g* with respect to Λ presents itself, which should be encapsulated in predictions for *g*. One of the first efforts in understanding the (k_s^+, Pr, Λ) dependency was conducted by Webb *et al.* (1971), where they performed experiments over two-dimensional (2-D) ribs. Although their data comprise, perhaps, the most comprehensive parameter sweep to date, e.g. $k_s^+ \approx 20–10^4$, $Pr = 0.7–37.6$, $\Lambda = 0.025–0.100$, their data are still ultimately restricted to mean-flow measurements like those in figure 1. Moreover, although their proposed correlation for the *g*-function in table 1 has been sensitised to Λ, this Λ dependency arises as a byproduct only by considering the drag $k_s/k = f(\Lambda)$, and does not treat the heat-transfer dependency on Λ explicitly. An understanding concerning the underlying physics associated with heat transfer and its dependency on Λ in particular, is still lacking.

It is well known that Λ is a crucial parameter in characterising rough-wall momentum transfer (drag) (e.g. Schlichting 1936; Fackrell 1984; Macdonald *et al.* 1998; Millward-Hopkins *et al.* 2011; Yang *et al.* 2016, 2022; Chung *et al.* 2021), with more recent literature on the effects of Λ on heat transfer now emerging (e.g. Miyake, Tsujimoto & Nakaji 2001; Ji, Yuan & Chung 2006; Leonardi *et al.* 2015; Forooghi, Stripf & Frohnapfel 2018*b*; Kuwata 2021; Yang *et al.* 2023). Notably, towards dense regimes ($\Lambda \gtrsim 0.3$), a phenomenon known as sheltering occurs, whereby separated flow downstream from roughness elements will impinge onto successive roughness elements. In the context of
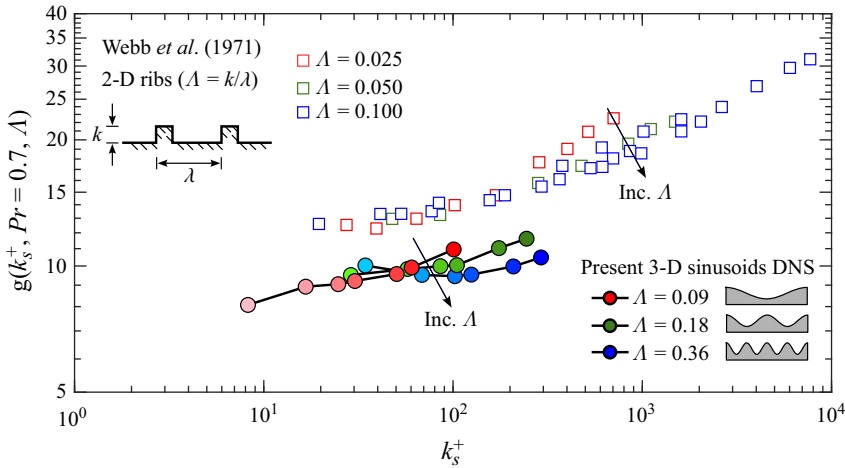
Figure 1. The influence of frontal solidity Λ on the (inverse) rough-wall heat transfer coefficient $g \equiv \Theta_{k_s}^+$, at fixed $Pr = 0.7$ for (circle markers with lines) our present DNS; (square markers) the experimental data of Webb *et al.* (1971).

drag, this effect has been investigated and modelled extensively (Macdonald *et al.* 1998; Millward-Hopkins *et al.* 2011; Yang *et al.* 2016; Busse, Thakkar & Sandham 2017), where the effects of flow sheltering will typically reduce drag in dense regimes (Chung *et al.* 2021). For heat transfer, Forooghi *et al.* (2018b) proposed that the sheltering effect may also have the same impact on the heat-transfer coefficient (Stanton number, C_h), owing to the weaker temperature gradients that tend to form in the low-speed, sheltered, wake regions. For example, the recent DNS of Kuwata (2021) varied Λ at a fixed $k_{rms}^+ = 17.0$ and fixed $Sk = 0.53$ or -0.53 for irregular rough surfaces, showing that $\Delta\Theta^+$ (corresponding to the change in C_h) increases with Λ regardless of Sk, consistent with the previously discussed trend of ΔU^+. The observations from the above cited studies suggest that a heat-transfer model in relation to the sheltering effect, akin to the progress in drag modelling (Macdonald *et al.* 1998; Millward-Hopkins *et al.* 2011; Yang *et al.* 2016), can be pursued once a systematic understanding of Λ and its influence on heat transfer is attained.

In view of the lack of understanding on the effects of the roughness height and density on drag and heat transfer, the present study aims to further understand the change of drag and the enhancement of heat transfer by systematically varying k^+ and Λ. For this purpose, we performed DNS using minimal channels, which can resolve the roughness sublayer at lower computational cost (MacDonald, Hutchins & Chung 2019), enabling access to the fully rough (high-k^+) regime at varying Λ, thereby providing an extensive data set to scrutinise.

In § 2, we outline our DNS set-up. In § 3, we showcase our present data, where we will argue that local rough-wall heat transfer can be understood through a simple decomposition between exposed and sheltered regions. Hinging on this finding, in § 4, we develop a predictive model for a rough-wall heat-transfer coefficient, i.e. $C_{h,k}(k^+, Pr, \Lambda)$.

2. Numerical methodology

This section describes the numerical methodology used in this study and is divided into two parts. First, descriptions of the flow configuration and the DNS algorithm are

provided (§ 2.1). Second, details of the three-dimensional (3-D) sinusoidal roughness and the simulation parameters are given (§ 2.2).

2.1. *Direct numerical simulations*

Direct numerical simulations of turbulent forced convection over 3-D roughness have been performed in an open-channel configuration. The continuity, Navier–Stokes and passive scalar transport equations solved in this study are

$$\frac{\partial u_i}{\partial x_i} = 0, \tag{2.1}$$

$$\frac{\partial u_i}{\partial t} + u_j \frac{\partial u_i}{\partial x_j} = -\Pi \delta_{1i} - \frac{1}{\rho} \frac{\partial p}{\partial x_i} + v \frac{\partial^2 u_i}{\partial x_j \partial x_j}, \tag{2.2}$$

$$\frac{\partial \theta}{\partial t} + u_j \frac{\partial \theta}{\partial x_j} = \alpha \frac{\partial^2 \theta}{\partial x_j \partial x_j} + Q, \tag{2.3}$$

where the velocity components in the streamwise (x), spanwise (y) and wall-normal (z) directions are u, v and w, respectively, and t is time. Buoyancy (due to gravity) and thermal expansion (β) properties of the fluid are neglected, i.e. $g\beta\Theta_\tau h/U_\tau^2 = 0$ (forced convection), and so temperature behaves as a passive scalar. The flow is driven through the open-channel domain by adding a spatially uniform body force to the right-hand side of the streamwise momentum equation, $\Pi \equiv -(1/\rho)\,\mathrm{d}P/\mathrm{d}x > 0$ (where ρ is density and $P(x)$ is the mean pressure). The hydrodynamic pressure that is solved for is the fluctuating (or periodic) component, p. To simulate forced convection, a body force was also added to the right-hand side of the transport equation for temperature, $Q = -u\,\mathrm{d}T_w/\mathrm{d}x > 0$, where u is the instantaneous streamwise velocity, $\mathrm{d}T_w/\mathrm{d}x$ is a prescribed mean wall-temperature gradient which drives the heat transfer and θ is the fluid temperature relative to the wall. This internal-heating technique can correspond to both a fluid moving along a cooled ($\mathrm{d}T_w/\mathrm{d}x < 0$, $\Theta > \Theta_w$, $\Theta_\tau > 0$) or heated ($\mathrm{d}T_w/\mathrm{d}x > 0$, $\Theta < \Theta_w$, $\Theta_\tau < 0$) wall and is a common forcing strategy amongst passive scalar channel-flow DNS (e.g. Kasagi, Tomita & Kuroda 1992; Alcántara-Ávila *et al.* 2021). Among both configurations, the dimensionless mean temperature $\Theta^+ \equiv (\Theta - \Theta_w)/\Theta_\tau$ remains the same. Our present framework adopts a prescribed temperature fluctuation $\theta = 0$ (Dirichlet) boundary condition at the wall, which, with our present choice of temperature forcing $Q = -u\,\mathrm{d}T_w/\mathrm{d}x$, can be shown to correspond to a statistically uniform wall heat flux (e.g. Kasagi *et al.* 1992; Kays *et al.* 2005) that mimics a Neumann boundary condition at the wall. For a statistically steady channel flow, volume integration shows that U_τ is related to the mean pressure gradient body forcing, Π, by $\Pi \equiv -(1/\rho)\,\mathrm{d}P/\mathrm{d}x = U_\tau^2/h$ (e.g. Pope 2000). This then enables a target value of $Re_\tau \equiv hU_\tau/v$ to be achieved by prescribing Π to set U_τ, for a given value of h and v. For our present temperature forcing $Q = -u\,\mathrm{d}T_w/\mathrm{d}x$, volume integration shows that the average wall heat flux is given by $\langle q_w \rangle/(\rho c_p) = hU_b(\mathrm{d}T_w/\mathrm{d}x)$, where $U_b \equiv (1/h)\int_0^h U\,\mathrm{d}z$ is the bulk velocity (e.g. Alcántara-Ávila *et al.* 2021). This then sets the friction temperature for normalisations of temperature quantities, $\Theta_\tau \equiv \langle q_w \rangle/(\rho c_p U_\tau)$. We imposed no-slip, impermeability conditions ($u = v = w = 0$), a zero fluid–wall temperature difference ($\theta = 0$) at the bottom wall and free slip, impermeable and adiabatic boundary conditions at the top boundary. Other internal-heating techniques are possible, e.g. a spatially uniform body force (Kim & Moin 1989; Pirozzoli, Bernardini & Orlandi 2016; Peeters & Sandham 2019). The average wall heat flux is defined here as $\langle q_w \rangle/(\rho c_p) = \alpha\langle\overline{\partial\theta/\partial n|_{wall}}\rangle$, where n is the local wall-normal direction, the overline

denotes temporal averaging and angle brackets denote an integral over the surface wetted area, normalised on the total plan area. The thermal diffusivity α is a property of the working fluid and is related to the molecular Prandtl number, $Pr \equiv \nu/\alpha$. Presently, we fix the Prandtl number to match that of air at standard atmospheric conditions, $Pr = 0.7$. The simulations have been run at a constant, prescribed bulk velocity as opposed to setting the pressure gradient forcing, Π. For each simulation, the bulk velocity is set by a trial and error procedure such that the friction Reynolds number, $Re_\tau \equiv U_\tau h/\nu$, matches its target value to within $\pm 1\%$. This latter step is done to set the value of the roughness Reynolds number $k^+ \equiv kU_\tau/\nu$ which, for our simulations, will be determined by $k^+ \equiv (k/h)Re_\tau$, where k/h is the inverse of the channel blockage ratio.

The governing equations (2.1) and (2.3) are solved using a low-storage third-order Runge–Kutta scheme (Spalart, Moser & Rogers 1991) in conjunction with a fractional step algorithm (Perot 1993), which was implemented in past work by Chung *et al.* (2015). Spatial discretisation is achieved using a fully conservative fourth-order symmetry preserving scheme (Verstappen & Veldman 2003). The passive scalar transport (2.3) is solved using a fourth-order implicit scheme for the wall-normal diffusive term, whereas the streamwise and spanwise terms are treated with an explicit scheme and advected using the Quadratic Upstream Interpolation for Convective Kinematics (QUICK) scheme (Leonard 1979). We have validated these discretisation schemes extensively in prior work applied to thermal convection configurations, demonstrating that both thermal dissipation (to 2%) and the global heat transfer (to 0.1%) are accurately captured provided the characteristic mesh size is at most two times larger than the Kolmogorov length scale $\eta \equiv (\nu^3/\varepsilon)^{1/4}$ for $Pr = 0.7$ where ε is the turbulent dissipation rate (table 2 Rouhi *et al.* 2021). For our present study, the most stringent resolution requirements are in the vicinity of the roughness and Zhong *et al.* (2023) reported that $\eta^+(z = k) \approx (\kappa k^+)^{1/4}$ in the fully rough regime for our present 3-D sinusoids at fixed $\Lambda = 0.18$. For our $k^+ \approx 33$–94, this yields an estimate $\eta^+(z = k) \approx 1.9$–$2.5$, which we amply resolve in the wall-normal direction ($\Delta z_w^+ \lesssim 1$, cf. table 2). This is relaxed in the streamwise grid resolution for instance, where we have used $\Delta x^+ \approx 7.3$–$9.9 > \eta^+(z = k)$. The roughness geometry is resolved using a direct-forcing variant of the immersed boundary method (IBM) based on a volume-of-fluid interpolation detailed in Rouhi, Chung & Hutchins (2019). Our present IBM code has been validated in earlier works for both momentum and heat transfer (Rouhi *et al.* 2019; Zhong *et al.* 2023). Periodic boundary conditions were enforced in the streamwise and spanwise directions. A free-slip boundary condition was enforced on the top boundary of the computational domain. A no-slip boundary condition was enforced on the bottom boundary using the IBM.

2.2. *Roughness geometry and simulation parameters*

The bottom boundary of the computational domain is covered with 3-D sinusoidal roughness (Chan *et al.* 2015), which follows a 2-D height distribution of the form

$$z_w(x, y) = k\cos(2\pi x/\lambda)\cos(2\pi y/\lambda), \tag{2.4}$$

where k is the semi-amplitude (i.e. half of the peak-to-trough height, $k_p/2$) and λ is the wavelength. The mean absolute height (k_a) and root-mean-squared height (k_{rms}) of the present 3-D sinusoids are constant multiples of its semi-amplitude, where $k = 2k_{rms} = (\pi^2/4)k_a$, whilst its skewness ($Sk$) is equal to zero (Chan *et al.* 2015). In addition, the effective slope (ES) of the present roughness can be expressed as $ES = (8/\pi)(k/\lambda)$, which is the mean absolute streamwise gradient of the height

W. Abu Rowin and others

	Colour	Re_τ	$\frac{h}{k}$	$\frac{\lambda}{k}$	$\frac{\lambda}{h}$	k^+	λ^+	L_x^+	L_y^+	N_x	N_y	N_z	Δx^+	Δy^+	Δz_w^+	Δz_h^+	$\frac{\lambda}{\Delta x}$	$\frac{\lambda}{\Delta y}$	$\frac{k_p}{\Delta z_w}$	$\frac{d}{k}$	$\frac{TU_\tau}{\min(z_c, h)}$
L		395	72	14.2	0.2	5.5	79	1256	471	384	288	225	3.27	1.64	0.12	3.45	24	48	92	0.02	25.9
		395	36	14.2	0.4	11.1	157	2513	1256	384	384	225	6.54	3.27	0.26	7.57	24	48	85	0.08	17.9
		590	36	14.2	0.4	16.5	235	3753	1877	512	512	300	7.33	3.67	0.38	6.19	32	64	87	0.13	19.7
		720	36	14.2	0.4	20.2	286	2290	859	256	192	350	8.95	4.47	0.38	6.74	32	64	106	0.18	19.3
		1200	36	14.2	0.4	33.6	477	3817	1431	384	288	450	9.94	4.97	0.60	7.38	48	96	112	0.18	17.6
		1440	36	14.2	0.4	40.3	573	4580	1718	496	360	450	9.23	4.77	0.77	8.42	62	120	105	0.18	16.5
		2400	36	14.2	0.4	67.2	954	7634	2862	768	576	900	9.94	4.97	0.77	12.3	96	192	175	0.12	8.68
M		395	36	7.1	0.2	11.1	79	1256	471	384	288	225	3.27	1.64	0.23	2.76	24	48	97	0.20	45.8
		395	18	7.1	0.4	22.1	157	2513	1256	384	384	225	6.54	3.27	0.51	6.05	24	48	87	0.19	14.1
		590	18	7.1	0.4	33.0	235	3753	1877	512	512	300	7.33	3.67	0.77	4.82	32	64	86	0.30	20.2
		720	18	7.1	0.4	40.3	286	2290	859	256	192	350	8.95	4.47	0.60	7.05	32	64	134	0.38	24.1
		1200	18	7.1	0.4	67.2	477	3817	1431	384	288	500	9.94	4.97	0.75	7.49	48	96	179	0.42	19.1
		1680	18	7.1	0.4	94.1	668	5344	2004	544	408	650	9.82	4.91	0.77	8.56	68	136	244	0.44	13.6
H		395	36	3.6	0.1	11.1	39	1256	393	768	480	225	1.63	0.82	0.23	2.76	24	48	97	0.45	28.0
		395	18	3.6	0.2	22.1	79	2513	393	768	240	225	3.27	1.64	0.51	6.05	24	48	87	0.45	39.1
		590	18	3.6	0.2	33.0	117	3753	586	768	240	300	4.89	2.44	0.77	4.82	24	48	86	0.46	38.7
		720	18	3.6	0.2	40.3	143	2290	716	384	240	350	5.96	2.98	0.77	7.33	24	48	105	0.50	19.7
		1200	18	3.6	0.2	67.2	239	3817	1193	384	240	500	9.94	4.97	0.77	7.27	24	48	175	0.52	25.1
		1680	18	3.6	0.2	94.1	334	5344	1670	544	340	650	9.82	4.91	0.77	8.56	34	68	244	0.54	17.8

Table 2. Simulation parameters for the nineteen rough-wall cases performed in this study. Sets L, M and H contain the low solidity ($\Lambda = 0.09$), medium solidity ($\Lambda = 0.18$) and high solidity ($\Lambda = 0.36$) cases, respectively. The simulation parameters include: the friction Reynolds number (Re_τ); the ratios of the open-channel mean height to the roughness semi-amplitude (h/k), the roughness wavelength to the roughness semi-amplitude (λ/k) and the roughness wavelength to the open-channel mean height (λ/h); viscous-scaled roughness height or roughness Reynolds number (k^+) and roughness wavelength (λ^+); viscous-scaled domain length (L_x^+) and width (L_y^+); number of grid points in the streamwise (N_x), spanwise (N_y) and wall-normal (N_z) directions; viscous-scaled streamwise (Δx^+), spanwise (Δy^+), wall-normal spacing within the roughness canopy (Δz_w^+) and at the open-channel mean height (Δz_h^+); number of grid points per roughness wavelength in the streamwise direction ($\lambda/\Delta x$), spanwise direction ($\lambda/\Delta y$) and number of grid points from the roughness peak-to-trough ($k_p/\Delta z_w$); the ratio of the virtual-origin shift to the roughness height (d/k); the non-dimensional sampling period ($TU_\tau/\min(z_c, h)$). Viscous-scaled quantities are non-dimensionalised using U_τ and ν.
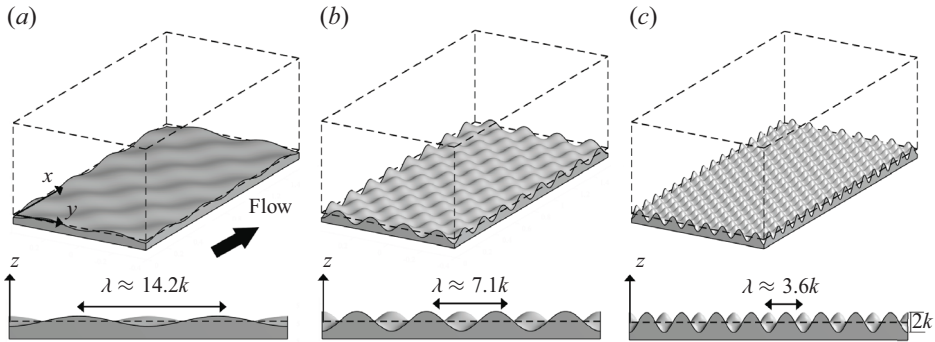
Figure 2. Open-channel-flow configuration with (*a*) low solidity ($\Lambda = 0.09$), (*b*) medium solidity ($\Lambda = 0.18$) and (*c*) high solidity ($\Lambda = 0.36$) sinusoidal roughness on the bottom boundary. The roughness mean plane is located at $z/h = 0$ and is shown as the dashed black line (- - -) on the side views.

distribution (Napoli, Armenio & De Marchis 2008), and is related to frontal solidity through the formula $\Lambda \equiv ES/2 = (4/\pi)(k/\lambda)$ (MacDonald *et al.* 2016). For a fixed roughness amplitude, a greater frontal solidity or, equivalently, a steeper *ES*, can be achieved by shortening the roughness wavelength. Alternatively, frontal solidity can be held constant by varying k and λ in proportion such that the geometric scaling factor k/λ remains fixed (Chan *et al.* 2018; Jelly *et al.* 2020). The present study directs attention to both techniques with the principal aim of understanding how systematic changes of frontal solidity affect heat and momentum transfer in rough-wall turbulent flow.

While turbulent forced convection over the present 3-D sinusoids has been investigated from smooth up to the fully rough regime in a minimal channel configuration by MacDonald *et al.* (2019), only a single value of frontal solidity of $\Lambda = 0.18$ was considered in their study. The present study builds upon the past work of MacDonald *et al.* (2019) by extending the investigation of turbulent forced convection over 3-D sinusoids to two new values of frontal solidity, namely, $\Lambda = 0.09$ and $\Lambda = 0.36$, in addition to the intermediate value of $\Lambda = 0.18$. Three-dimensional sketches of the sinusoidal roughness for each value of frontal solidity considered here are shown in figure 2. The three solidity cases $\Lambda = 0.09$, 0.18 and 0.36 are obtained by varying the roughness wavelength as $\lambda \approx 14.2k$, $7.1k$ and $3.6k$ shown in figures 2(*a*), 2(*b*) and 2(*c*), respectively.

Table 2 details the simulation parameters for the nineteen rough-wall cases considered in this study. The simulations have been grouped into three separate sets according to their frontal solidity as low (L), medium (M) and high (H) corresponding to $\Lambda = 0.09$, 0.18 and 0.36. Set L contains the low solidity cases $\Lambda = 0.09$, which falls into the sparse regime of $\Lambda < 0.18$, as shown by MacDonald *et al.* (2016) for similar roughness geometry. This set has a blockage ratio of $h/k = 36$, except for one case where $h/k = 72$ to ensure that $Re_\tau \gtrsim 395$ for all cases to minimise low-Reynolds-number pressure gradient effects (Nickels 2004). The roughness Reynolds number, $k^+ \equiv kU_\tau/\nu$, for this set covers $5 \lesssim k^+ \lesssim 67$. Set M contains the medium solidity cases ($\Lambda = 0.18$), which has a blockage ratio of $h/k = 18$, except for one case where $h/k = 36$, and covers the roughness Reynolds-number range $11 \lesssim k^+ \lesssim 94$. Set H contains the high solidity cases $\Lambda = 0.36$, which falls into the dense regime of $\Lambda > 0.18$ (MacDonald *et al.* 2016), which also has a blockage ratio of $h/k = 18$, except for one case where $h/k = 36$, and covers the roughness Reynolds-number range $11 \lesssim k^+ \lesssim 94$. Past work by Chan *et al.* (2015) and Chung *et al.* (2015) fitted the data of the present 3-D sinusoidal roughness with $\Lambda = 0.18$ in the fully rough regime, obtaining an equivalent sand-grain roughness of

$k_s \approx 4.1k$. Based on this previously obtained value, the group M cases span the range of $21 \lesssim k_s^+ \lesssim 268$ and encompass both the transitionally and fully rough regimes. The ratio of k_s/k will be further investigated in § 3.3 after applying the virtual-origin shift. To reduce the computational cost of achieving fully rough conditions (which is needed to compute an equivalent sand-grain roughness for groups L and H), the spanwise domain width, L_y, was kept narrow in the spirit of the minimal channel for rough-wall flows proposed by Chung *et al.* (2015). Although restricting the spanwise channel width produces unphysical results in the outer layer (e.g. the formation of an artificial wake), the near-wall flow remains unaffected and closely resembles a full-span simulation up to a wall-normal critical height of $z_c \approx 0.4L_y$ (Flores & Jiménez 2010). For all cases considered here, the spanwise domain width accommodates a minimum of three roughness wavelengths ($L_y/\lambda = 3$), which is a factor of three wider than that used by MacDonald *et al.* (2019). The spanwise extent of our computational domain therefore satisfies the recommendations made by Chung *et al.* (2015), namely $L_y \gtrsim \max(100\nu/U_\tau, k/0.4, \lambda)$. In addition, our present choice of L_y also ensures the minimal channel critical height, $z_c = 0.4L_y$ is greater than the roughness sublayer thickness estimated as $z_r \approx 0.5\lambda$ for our present roughness based on the wall-normal extent of roughness-induced dispersive motions (Chan *et al.* 2018). The $z_c > z_r$ condition then ensures that the near-wall roughness sublayer flow is correctly resolved by our minimal channels. The critical height z_c also applies to the temperature field, as shown by MacDonald *et al.* (2019) and Zhong *et al.* (2023). The streamwise domain lengths used throughout this study also satisfy the condition $L_x \gtrsim \max(3L_y, 1000\nu/U_\tau, \lambda)$, as recommended by MacDonald *et al.* (2017). For the wall-normal grid, a uniform grid spacing of Δz_w^+ is used from the roughness trough ($z/k = -1$) up to the roughness peak ($z/k = 1$), before being gently stretched to a maximum value of Δz_h^+ at the top boundary of the open-channel domain ($z/h = 1$) using a hyperbolic tangent function. The peak-to-trough height of the roughness canopy ($k_p \equiv 2k$) is resolved using a minimum of eighty-five points ($k_p/\Delta z_w \gtrsim 85$). Uniform grid spacing is used in the streamwise and spanwise directions, which ranges from $3.3 < \Delta x^+ < 9.9$ and $0.8 < \Delta y^+ < 5.4$ for all cases considered here. In line with past recommendations made by Chan *et al.* (2015), the roughness topography was resolved using a minimum of twenty-four points per wavelength in the streamwise direction ($\lambda/\Delta x = 24$, where Δx is the streamwise grid spacing) and a minimum of forty-eight points per wavelength in the spanwise direction ($\lambda/\Delta y = 48$, where Δy is the spanwise grid spacing). Further details are given in table 2. Validation of the current simulations against the past work of MacDonald *et al.* (2019) using a different (finite volume) solver at matched medium solidity ($\Lambda = 0.18$) is included in Appendix A. Statistical quantities were computed using a space-then-time averaging methodology. Specifically, an instantaneous field variable, say, $\phi(x, y, z, t)$, was first spatially averaged across the xy-plane at each wall-normal height and then time averaged. Only in-fluid cells contribute to spatially averaged quantities within the roughness canopy ($-1 < z/k < 1$), which corresponds to an intrinsic average (Gray & Lee 1977). Throughout this manuscript, $U(z)$ and $\Theta(z)$ denote the mean streamwise velocity and mean fluid temperature relative to the wall respectively. Statistical quantities reported herein were collected for a minimum of fifteen large-eddy turn over times, depending on the spanwise domain width and the friction Reynolds number.

3. Results and discussion

In this section we first show the influence of the virtual origin (§ 3.1). Then, we present the effect of the solidity and the roughness Reynolds number k^+ on the mean profiles

(§ 3.2) and roughness functions (§ 3.3). Lastly, we provide a local view to the flow and heat-transfer behaviour, using these observations to motivate a model (§ 3.4).

3.1. *Investigation of the virtual origin*

The virtual origin could have a significant impact on the obtained results, especially for large k^+ (Perry, Schofield & Joubert 1969). Several frameworks have been proposed for the virtual-origin offset, d, such as: the logarithmic origin (Perry & Joubert 1963; Perry *et al.* 1969), the moment of forces acting on the roughness elements (Jackson 1981) or the Reynolds shear stress for transitionally rough surfaces (Luchini 1996; Luchini & Quadrio 2022). Significant effort has been directed towards implementing and improving the previous techniques such as Chan *et al.* (2015), Abderrahaman-Elena, Fairhall & García-Mayoral (2019) and Ibrahim *et al.* (2021). Prior works that have considered an identical 3-D sinusoidal topography to the present work (Chan *et al.* 2018; MacDonald *et al.* 2019) have neglected any virtual-origin influences, instead taking the origin to be the roughness midplane. To understand the sensitivity of the following results on the virtual-origin shift (d), we first estimate d as the value that yields to a close approximation of $\kappa = 0.4$ in the logarithmic region of the mean velocity profiles. We note the uncertainties that may arise in adopting this approach, as a more recent high-Reynolds-number DNS has shown that $\kappa \approx 0.38$–0.39 (Lee & Moser 2015; Pirozzoli *et al.* 2021; Hoyas *et al.* 2022), and that our present lowest $Re_\tau \approx 395$ may not provide robust logarithmic regions, all of which will contribute to uncertainties in how we obtain d. As we will see, however, in figure 3, these uncertainties in the precise measurement of d will not be important when considering the overall trends of ΔU^+, $\Delta \Theta^+$. Presently, we define the limits of the logarithmic region to estimate d as the roughness sublayer thickness for the lower limit, $z_r - d \approx 0.5\lambda$ (Chan *et al.* 2018) and the upper limit as $0.2h$ (Marusic & Monty 2019). The lower limit for the logarithmic region based on the roughness influence at 0.5λ may still be within the buffer layer for cases where λ^+ is small (i.e. high solidity, low k^+). However, even when we restrict the lower limit of the logarithmic region to $\max(0.5\lambda^+, 50)$, we find that the variation in d/k does not exceed 0.02. To also ensure that a logarithmic region with a substantial wall-normal distance (of at least 40 wall units) is maintained, it is sometimes necessary to extend the upper limit of the logarithmic region beyond $0.2h$, especially in low-Reynolds-number cases. For example, when dealing with groups L and M where $Re_\tau = 590$, the upper limit of the logarithmic region is extended to $0.3h$. Figure 3(a) shows the ratio of d to the roughness height k, for groups L, M and H as a function of k^+. The ratios of d/k are also listed in table 2.

Figure 3(a) shows that d is confined between the roughness mid-plane and crest $0 \lesssim d/k \lesssim 1$. We have also included recent data from the DNS of Zhong *et al.* (2023). This work adopted an identical 3-D sinusoidal roughness to the present study, with a fixed value of $\Lambda = 0.18$. The authors obtained d through a similar *ad hoc* fit to the logarithmic regions, wherein the fitting was adjusted to match both the logarithmic mean velocity and temperature slopes, which were approximately $\kappa \approx 0.4$ and $\kappa_h \approx 0.47$, respectively. In contrast, the present work only tunes to match $\kappa \approx 0.4$, resulting in slightly different values of d that are evident in figure 3(a). While there are noted limitations in accurately estimating d across the investigated k^+ range, any potential variations in d are not found to significantly influence our conclusions. This observation is supported in figure 3(b), wherein the error bars for the velocity and temperature roughness functions, denoted as ΔU^+ and $\Delta \Theta^+$ respectively, are plotted for groups L, M and H, representing the uncertainty due to situating the virtual origin at the roughness crests ($d = k$) and midplane
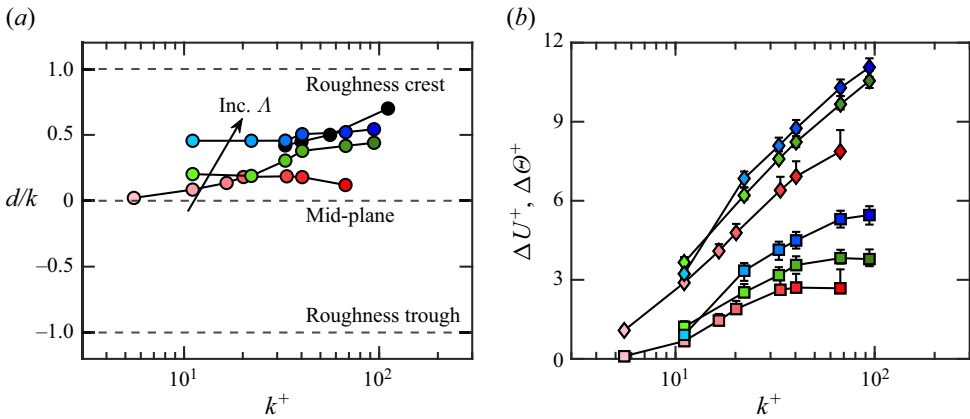
Figure 3. (*a*) The ratio of the virtual origin to the roughness height (d/k) as a function of k^+ for low ($\circ$, red), intermediate ($\circ$, green) and high ($\circ$, blue) solidity cases. Results of d/k of Zhong *et al.* (2023) for 3-D sinusoidal roughness with $\Lambda = 0.18$ and $k^+ = 33, 40, 56, 111$ ($\bullet$) are also included in (*a*) for comparison. (*b*) Roughness function of velocity, ΔU^+, (diamond markers) and temperature, $\Delta \Theta^+$ (square markers) against k^+. The darker shaded markers refer to increasing roughness height k^+, while the error bars refer to the uncertainty of estimating ΔU^+ and $\Delta \Theta^+$ due to selection of extreme virtual origin values of $d = [0, k]$.

($d = 0$). Error bars are also included in this figure to present the uncertainty in ΔU^+ and $\Delta \Theta^+$ due to selecting extreme bounds of the virtual origin, where $d = k$ and $d = 0$ at the roughness crest and trough, respectively. The effect of varying d from the roughness crest to roughness mid-plane causes a maximum of $\sim 6\,\%$ relative error for ΔU^+ and $\sim 12\,\%$ for $\Delta \Theta^+$ for $k^+ = 94.1$ and $\Lambda = 0.36$. Despite these extreme limits, we observe from figure 3(*b*) that the overall trends of ΔU^+ and $\Delta \Theta^+$ are robust. Hereafter, for definiteness and simplicity we will present data with d obtained from fitting the logarithmic region $[0.5\lambda, (0.2 - 0.3)h]$ to a best-fit logarithmic slope of $\kappa = 0.4$. The same d values obtained from fitting the slopes of the logarithmic region of the velocity profiles are used for the temperature data.

The uncertainty of d/k also influences the ratio of k_s/k. Here, k_s is the equivalent sand-grain roughness height obtained by overlaying the current ΔU^+ with the fully rough asymptote (1.2). For example, for group M, the ratio k_s/k is expected to change from $k_s/k \approx 1.9$ at $d = k$ to $k_s/k \approx 2.8$ at $d = 0$. The sensitivity of k_s/k to d could explain the difference between k_s/k of the current data and other simulations over 3-D sinusoidal surface (with $\Lambda = 0.18$) such as $k_s/k = 4.1$ of Chan *et al.* (2015) and $k_s/k = 3.7$ of Ma *et al.* (2020), although other parameters like the blockage ratio and the logarithmic-law constants (κ and A) will also impact k_s/k.

3.2. *Mean profiles*

The normalised mean streamwise velocity profiles, U^+, vs the inner-scaled wall-normal distance, z^+, for the low (L), intermediate (M) and high (H) solidity groups are shown in figure 4(*a,c,e*). Details of the three solidity groups are listed in table 2. As expected, the increase of the roughness Reynolds number, k^+, creates an increasing downward shift within the logarithmic region limits, corresponding to an increase of the velocity roughness function, ΔU^+. This trend remains consistent irrespective of the roughness solidity. The downward shift is more pronounced at the higher solidity (see figure 4*e*). The insets of figure 4(*a,c,e*) show the difference between the reference smooth-wall DNS
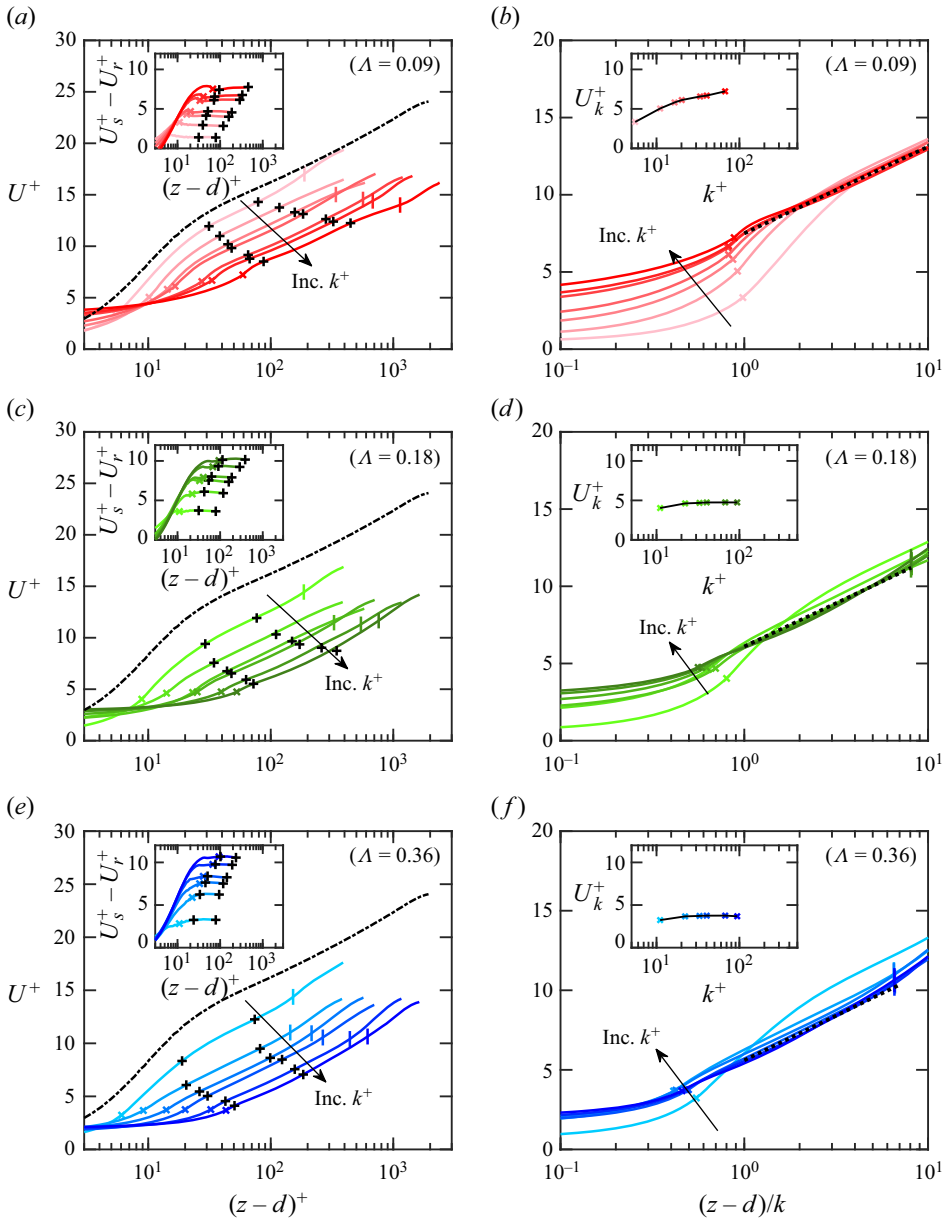
979 A22-12

Figure 4. Viscous-scaled mean velocity, U^+, against (a,c,e) $(z-d)^+$ and (b,d,f) $(z-d)/k$. The solid lines are rough-wall open channels for low solidity $\Lambda = 0.09$ (a,b), medium solidity $\Lambda = 0.18$ (c,d) and high solidity $\Lambda = 0.36$ (e,f). The darker shaded lines and markers refer to increasing roughness height (k^+) as listed in table 2. The black dot-dashed line in (a,c,e) is the smooth-wall profile from the DNS of Bernardini, Pirozzoli & Orlandi (2014). The fully rough asymptote $(U^+ = \kappa^{-1} \log[(z-d)/k] + C_{FR})$ is shown with the black dotted lines in (b,d,f), where $C_{FR} = \{2.6, 4.0, 4.5\}$ for $\Lambda = \{0.09, 0.18, 0.36\}$. The velocity difference between the smooth wall of Bernardini *et al.* (2014), U_s^+, and the rough wall, U_r^+, is shown in the insets in (a,c,e) for each corresponding solidity case. The velocity at the roughness crest U_k^+ (cross marks, $\times$) vs k^+ is also shown in the insets in (b,d,f). The vertical marks show the critical height $z_c^+ = 0.4L_y^+$. The limits of the logarithmic region are shown with plus marks, $+$, in (a,c,e) and their corresponding insets.

velocity profile, U_s^+, of Bernardini *et al.* (2014) and the velocity profile for the rough walls, U_r^+. The flat portions depicted in these insets signify the presence of a logarithmic region over the rough cases with a slope (κ^{-1}) comparable to that of the smooth wall, and are a result of our manual tuning of d in §3.1 to match the smooth-wall κ^{-1} slope. The logarithmic region limits, as indicated by the black plus marks in figure 4, are the same as those used in §3.1 to determine d. These limits will be utilised to compute the velocity and temperature roughness functions in §3.3. The crest velocity U_k^+ retains a constant value for $k^+ \gtrsim 20$ in the insets of figures 4(*d*) and 4(*f*), suggesting fully rough conditions have been attained for $\Lambda = 0.18$ and $\Lambda = 0.36$ (Flack & Schultz 2010). However, the non-constant U_k^+ for the lowest solidity case $\Lambda = 0.09$ in the inset of figure 4(*b*) suggests that the attainment of fully rough conditions in this case is uncertain.

The mean temperature normalised by the friction temperature, $\Theta^+ = \Theta/\Theta_\tau$ as a function of $(z - d)^+$ for the three solidity cases is shown in figures 5(*a*), 5(*c*) and 5(*e*). The temperature profile of Pirozzoli *et al.* (2016) for a smooth wall is also included for comparison. The increase of k^+ leads to increasing downward shifts in the logarithmic region of the mean temperature profile, although this seems to plateau at $k^+ = 33.6$, 40.3 and 67.2 for $\Lambda = 0.09$, 0.18 and 0.36, respectively. Beyond this, the increase in k^+ results in comparable temperature profiles in the logarithmic region. This change in the shift between the temperature profile of smooth and rough walls suggests a slow down of the increase of the temperature roughness function, $\Delta\Theta^+$ with increasing k^+, as previously reported by MacDonald *et al.* (2019) and Peeters & Sandham (2019) and embodied in the models suggested by Owen & Thomson (1963), Brutsaert (1975) and Yaglom & Kader (1974). More details about the velocity and temperature roughness functions are given in §3.3. The increase in the solidity has a clear effect on the shift between the smooth- and rough-wall-temperature profiles even at a comparable k^+. This is clearly illustrated in the insets of figure 5(*a,c,e*), where $(\Theta_s^+ - \Theta_r^+) \approx 2.5$ and ≈ 5.1 for $\Lambda = 0.09$ and $\Lambda = 0.36$, respectively, at $k^+ \approx 67$ (see insets in figure 5*a,e*). The greater downward shift of Θ^+ at higher Λ hints at higher heat transfer at higher Λ. A similar increase in heat transfer with increasing Λ was reported for the fixed-skewness fully rough irregular surfaces of Kuwata (2021). The temperature profiles Θ^+ for the three solidity cases within the roughness canopy $(z - d)/k \lesssim 1$ are shown in figure 5(*b,d,f*). Regardless of the solidity, Θ^+ increases with k^+ within the roughness canopy. The location of the roughness crest is marked with the '×' symbols in figure 5(*b,d,f*). This observation is consistent with increased mixing from eddies that straddle the logarithmic region near the crest with temperature Θ_k^+ down into the roughness canopies, as allowed by the increasing and sufficiently large k^+. Here, $\Theta_k^+ \equiv \Theta^+(z = k)$ denotes the crest temperature. The insets in figure 5(*b,d,f*) present a logarithmic increase of Θ_k^+ (and is also listed in table 3) with increasing k^+. This trend was also documented previously by MacDonald *et al.* (2019). All three solidities show the same trend of increasing peak temperature with increasing k^+, with the lowest solidity $\Lambda = 0.09$ exhibiting the greatest rate of increase.

3.3. *Roughness function*

The velocity (ΔU^+) and temperature ($\Delta\Theta^+$) roughness functions are presented in figure 6, plotted against k_s^+ in (*a,c*) and against Λ in (*c,d*). The roughness functions here are estimated as the averages of $(U_s^+ - U_r^+)$ and $(\Theta_s^+ - \Theta_r^+)$ within the logarithmic region as indicated by the black plus marks in figures 4 and 5. Error bars are included in figure 6(*a,b*), which show the maximum observed deviation for each case for virtual-origin values of $d = [0, k]$. The ratio of k_s/k for figure 6(*a,c*) is estimated directly by overlaying the current
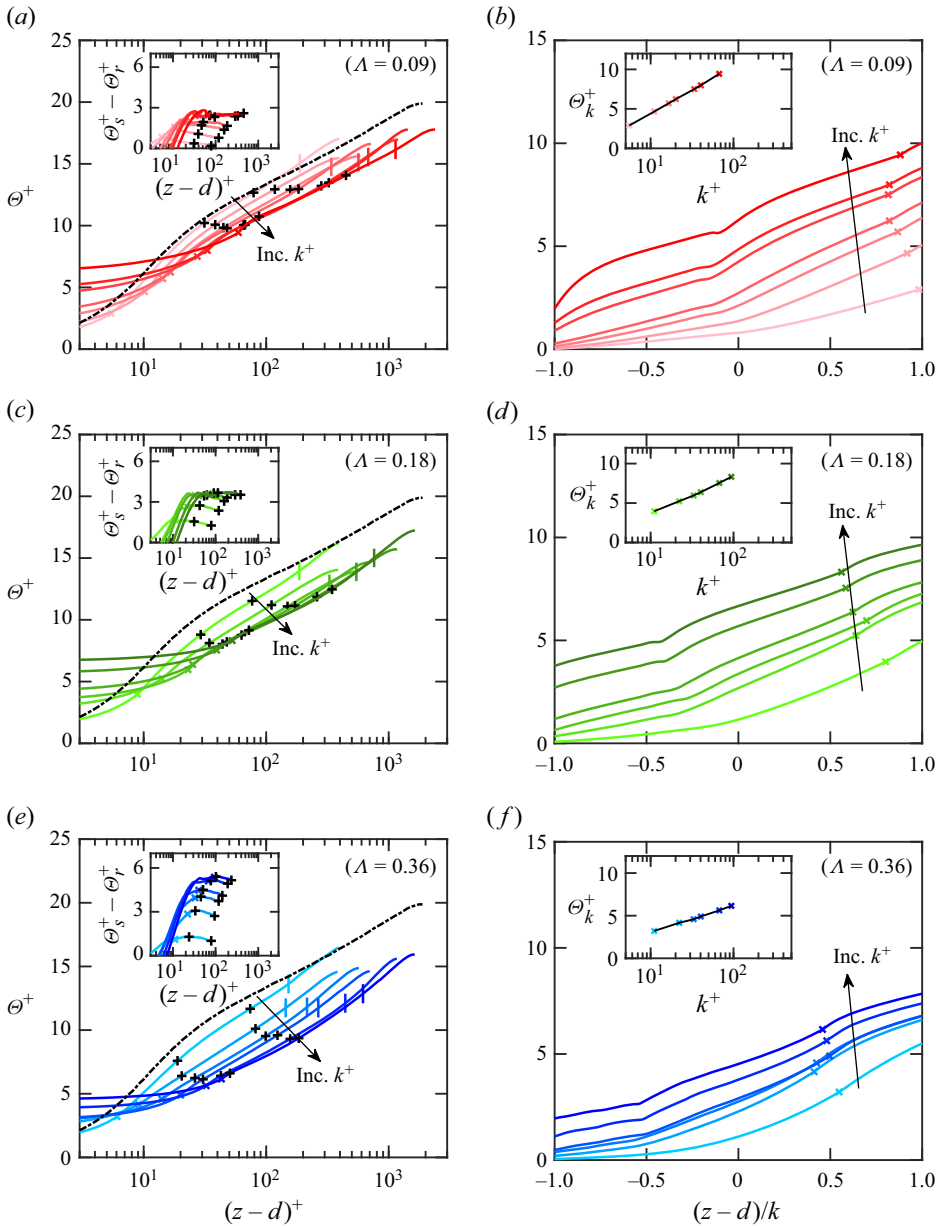
Figure 5. Viscous-scaled mean temperature against (a,c,e) $(z-d)^+$ and (b,d,f) $(z-d)/k$. The solid lines are rough-wall open channels for low solidity $\Lambda = 0.09$ (a,b), medium solidity $\Lambda = 0.18$ (c,d) and high solidity $\Lambda = 0.36$ (e,f). The darker shaded lines and markers refer to increasing roughness height (k^+) as listed in table 2. The black dot-dashed line in (a,c,e) is the smooth-wall profile from the DNS of Pirozzoli *et al.* (2016). The temperature difference between the smooth wall of Pirozzoli *et al.* (2016), Θ_s^+, and the rough wall, Θ_r^+, is shown in the insets in (a,c,e) for each corresponding solidity case. The temperature at the roughness crest Θ_k^+ (cross marks, $\times$) vs k^+ is also shown in the insets in (b,d,f). The vertical marks show the critical height $z_c^+ = 0.4L_y^+$. The limits of the logarithmic region are shown with plus marks, $+$, in (a,c,e) and their corresponding insets.

	k^+	C_f	C_h	ΔU^+	$\Delta \Theta^+$	U_k^+	Θ_k^+	Θ_{ks}/Θ_k
	5.5	0.0060	0.0034	1.41	0.28	3.34	2.90	1.58
	11.1	0.0071	0.0039	2.88	0.88	5.05	4.65	1.46
	16.5	0.0073	0.0039	4.06	1.53	5.82	5.70	1.36
L	20.2	0.0074	0.0039	4.65	1.82	6.12	6.23	1.31
	33.6	0.0076	0.0038	6.16	2.43	6.57	7.50	1.22
	40.3	0.0077	0.0038	6.70	2.48	7.68	7.98	1.20
	67.2	0.0074	0.0035	7.67	2.52	7.22	9.44	1.15
	11.1	0.0078	0.0042	3.67	1.29	4.03	3.96	2.14
	22.1	0.0107	0.0053	6.01	2.53	4.62	5.24	1.74
	33.0	0.0114	0.0055	7.43	3.25	4.68	5.96	1.58
M	40.3	0.0115	0.0054	7.97	3.44	4.74	6.38	1.51
	67.2	0.0117	0.0051	9.30	3.62	4.74	7.54	1.39
	94.1	0.0119	0.0049	10.24	3.65	4.74	8.32	1.34
	11.1	0.0074	0.0041	3.23	0.91	3.23	3.21	2.84
	22.1	0.0111	0.0056	6.74	3.21	3.67	4.16	2.18
	33.0	0.0117	0.0058	7.97	4.02	3.72	4.58	1.98
H	40.3	0.0121	0.0059	8.75	4.49	3.75	4.90	1.87
	67.2	0.0125	0.0058	10.29	5.30	3.75	5.63	1.70
	94.1	0.0127	0.0057	11.07	5.46	3.68	6.16	1.64

Table 3. Bulk flow properties for the nineteen rough-wall cases simulated in this study including the expected full-span skin-friction coefficient and Stanton number defined on the centreline values $U_h^+ \equiv U^+(z = h)$ of (1.1), $\Theta_h^+ \equiv \Theta^+(z = h)$ of (1.3), ($C_f \equiv 2/(U_h^+)^2$ and ($C_h \equiv 1/(U_h^+ \Theta_h^+)$)); roughness functions (ΔU^+, $\Delta \Theta^+$); the velocity at the roughness crest (U_k^+); the temperature at the roughness crest (Θ_k^+) and the ratio of the temperature at $z - d = k_s$ and $z = k$ (Θ_{ks}/Θ_k) used to pass from the g-function (1.3b) to the rough-wall heat transfer coefficient $C_{h,k}$ (§ 4).

results for $\Delta U^+(k^+)$ with that of the sand-grain roughness of Nikuradse (1933) or with (1.2). The ratio of k_s/k could also be computed from

$$\frac{k_s}{k} \approx \exp\left[\kappa(C_N - C_{FR})\right], \tag{3.1}$$

where $C_N \approx 8.5$ is the Nikuradse fully rough intercept for sand-grain roughness and C_{FR} is the offset of the fully rough asymptote for the current data as shown in figure 4(b,d,f). For $\Lambda = 0.09$, 0.18 and 0.36, $k_s/k \approx 1.6$, 2.7 and 3.5, respectively. It is worth noting that the value of k_s/k for $\Lambda = 0.09$ is perhaps uncertain as it is not clear whether fully rough conditions have been achieved. Also, it is important to highlight that the ratio of k_s/k is anticipated to change with the virtual origin. For instance, when $d = 0$ (implying that the origin is at the roughness semi-amplitude) and for $\Lambda = 0.18$, $k_s/k \approx 2.8$, as discussed in Appendix A. The increase of k_s/k with Λ could be attributed to the monotonic increase of ΔU^+ with Λ previously seen in Yuan & Piomelli (2014), Kuwata & Nagura (2020) and Kuwata (2021). Waigh & Kind (1998) also suggested that $k_s/k \approx X\Lambda^a$, where X and a are constants depending on the roughness structure. For the current 3-D sinusoidal roughness, $k_s/k \approx 6.2\Lambda^{0.55}$. For an identical 3-D sinusoidal topography in pipe flows, Chan *et al.* (2015) found $k_s/k \approx 10\Lambda^{0.45}$.

Figure 6(a) demonstrates that ΔU^+ follows the fully rough asymptote (1.2) beginning at $k_{s,FR}^+ \approx 64$, 100 and 235 for $\Lambda = 0.09$, 0.18 and 0.36. For $k_s^+ < k_{s,FR}^+$ (i.e. aerodynamically smooth and transitionally rough regimes), ΔU^+ for the three solidity cases do not overlap,
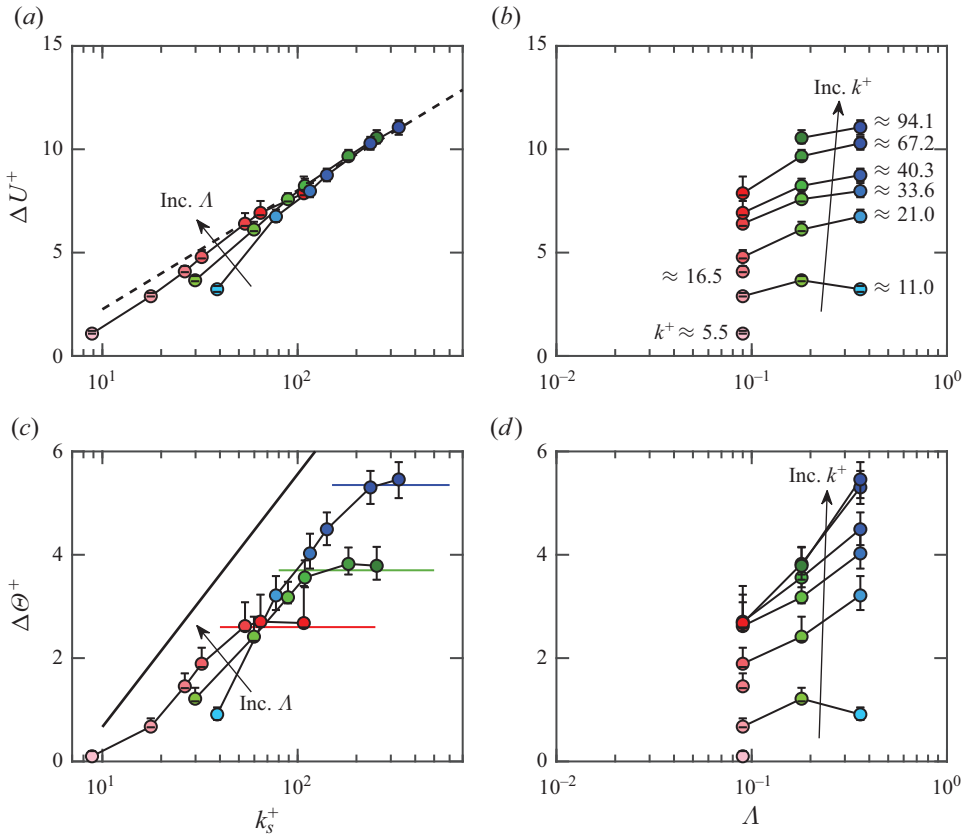
979 A22-16

Figure 6. Velocity roughness function ΔU^+ as a function of (a) k_s^+ and (b) Λ and temperature roughness function $\Delta\Theta^+$ as a function of (c) k_s^+ and (d) Λ for low ($\circ$, red), intermediate ($\circ$, green) and high ($\circ$, blue) solidity cases. The darker shaded markers refer to increasing k^+. The dashed line in (a) is the fully rough asymptote (1.2). In (c), the solid line is (3.2) assuming the value of term 2 is zero. The horizontal lines in (c) represent the values of $\Delta\Theta^+$ corresponding to the anticipated initiation of fully rough behaviour, specifically $k_{s,FR}^+ \approx 64$, 100 and 235 for $\Lambda = 0.09$, 0.18 and 0.36, respectively.

indicating that the solidity also plays a strong role in determining drag behaviour in the transitionally rough regime, a consistent finding with the transitionally rough literature (Chung *et al.* 2021).

The influence of Λ in different roughness regimes can be examined in figure 6(b), which plots ΔU^+ against Λ for different k^+. For the transitionally rough regime at $k^+ \approx 11$, ΔU^+ increases with Λ up to the limit of the sparse regime $\Lambda \lesssim 0.18$. Beyond this range, where the dense regime starts $\Lambda \gtrsim 0.18$, ΔU^+ decreases. This trend was previously reported by MacDonald *et al.* (2016) with matched roughness geometry and $k^+ = 10$ (also in the transitionally rough regime). MacDonald *et al.* (2016) and Sharma & García-Mayoral (2020) related this trend to the reduction of the spacing between roughness elements in viscous units and thus at very high solidities the eventual establishment of an effective smooth wall at the roughness crest. It is noteworthy that, for $k^+ \gtrsim 21$, ΔU^+ exhibits a monotonically increasing trend with increasing Λ at matched k^+. This finding is in contrast to the peak behaviour of ΔU^+ that occurs between dense and sparse density regimes as observed at $k^+ \approx 11.0$. The monotonic increase of ΔU^+ with Λ trend was also previously observed in Yuan & Piomelli (2014), Kuwata & Nagura (2020) and

Kuwata (2021). Kuwata (2021) attributes the monotonically increasing trend of ΔU^+ with Λ for fixed-skewness fully rough surfaces to the increase of pressure drag at higher values of Λ.

In contrast to the trend in figure 6(*b*), where ΔU^+ approaches a plateau at high Λ and k_s^+, figure 6(*d*) indicates that $\Delta \Theta^+$ increases sharply with Λ at high k^+. An extrapolation of these observations implies that a rough wall operating in the fully rough regime with very high Λ could potentially yield a $\Delta \Theta^+$ that approached ΔU^+. Previous investigations conducted by Forooghi, Magagnato & Frohnapfel (2018*a*) and Forooghi *et al.* (2018*c*), which involved simulations and analysis of irregular roughness, suggested that the variations in heat transfer with respect to Λ may be attributed to a sheltering mechanism. In the subsequent section, we will focus on examining the validity of this hypothesis by analysing the local heat-transfer variations and their relationship to flow conditions involving sheltered and exposed regions.

An interesting observation arising from the comparison between figures 6(*a*) and 6(*c*) is that the onset of fully rough drag, characterised by $k_{s,FR}^+$, roughly coincides with the point whereby $\Delta \Theta^+$ no longer continues to increase with k_s^+ and instead, attains a peak value. For $k_s^+ < k_{s,FR}^+$, an analogous behaviour between rough-wall heat and momentum transfer ($\Delta \Theta^+$ and ΔU^+) persists, whereby both continually increase with k_s^+. Once $k_s^+ \geq k_{s,FR}^+$, a pronounced breakdown in this heat and momentum transfer analogy begins, and, since $k_{s,FR}^+$ depends on Λ, the onset of this pronounced breakdown is therefore dependent on Λ. The horizontal lines in figure 6(*c*) illustrate that the value of $\Delta \Theta^+$ at $k_{s,FR}^+$ serves as a reliable approximation for the peak value of $\Delta \Theta^+$. This breakdown in the analogy between ΔU^+ and $\Delta \Theta^+$ may also be viewed in the context of the widely employed canonical Reynolds-analogy prediction in engineering, expressed as $C_f/2 \approx C_h$, the $Pr = O(1)$ approximation to the Chilton–Colburn relation $C_f/2 \approx C_h Pr^{2/3}$ (Chilton & Colburn 1934). Here, C_f and C_h represent the bulk skin friction and Stanton number, respectively (as defined below) (Kays *et al.* 2005). By manipulating the logarithmic laws for velocity (1.1) and temperature (1.3) it is possible to establish an explicit relation between $\Delta \Theta^+$ and its association with ΔU^+

$$\Delta \Theta^+ = \underbrace{A_h - Pr_t A + Pr_t \Delta U^+}_{term\ 1} - \underbrace{\left(\frac{C_f}{2C_h} - Pr_t \right) \sqrt{\frac{2}{C_f}}}_{term\ 2}, \tag{3.2}$$

where $C_f \equiv \langle \tau_w \rangle / (\rho U_h^2/2) \equiv 2/(U_h^+)^2$ and $C_h \equiv \langle q_w \rangle / (\rho c_p U_h \Theta_h) \equiv 1/(U_h^+ \Theta_h^+)$ are the bulk skin-friction coefficient and Stanton number, respectively, which are defined on the logarithmic velocity and temperature evaluated at the channel centreline, i.e. $U_h^+ \equiv U^+(z = h)$, $\Theta_h^+ \equiv \Theta^+(z = h)$. Values for C_f and C_h, extrapolated for minimal channel simulations using (1.1) and (1.3), are reported in table 3. Equation (3.2) is obtained by evaluating (1.1), (1.3) at $z = h$ and combining the results to eliminate the logarithmic term. Two aggregated terms may be identified in (3.2), term 1, which includes inner-scale quantities associated with the log region that are invariant with respect to an outer-scale Reynolds number, $Re \equiv 2hU_h/\nu$ provided outer-layer similarity holds; and term 2: outer-scale quantities involving C_f, C_h. While C_f and C_h exhibit inherent dependencies on Re (Kays *et al.* 2005), it is noteworthy that term 2 in (3.2) remains independent of Re in its entirety. Consequently, it qualifies as an inner-scaled quantity due to the fact that $\Delta \Theta^+$, being an inner-scaled quantity itself, is a function of k_s^+, Pr and Λ, rather than Re. Here, (3.2) provides an explicit avenue to invoke

Reynolds analogy $C_f/(2C_h) \approx 1.0 \approx Pr_t$ (thereby eliminating term 2) and examine its consequences on $\Delta\Theta^+$ in relation to ΔU^+. For constants in (3.2), we use $A_h(Pr = 0.7) \approx 3.6$, $A \approx 5.0$, $Pr_t \approx 0.85$ and (1.2) for ΔU^+. The resulting curve for $\Delta\Theta^+$ adopting the Reynolds-analogy assumption is shown by the solid black line in figure 6(*c*). Clearly, the data deviate from this curve, indicating that rough walls do not adhere to Reynolds analogy ($C_f/2 \neq C_h$), a well-established finding in rough-wall heat-transfer literature (e.g. Dipprey & Sabersky 1963). Nevertheless, valuable insights can still be gleaned by comparing the data with this Reynolds-analogy curve. Specifically, in the transitionally rough regime, where $k_s^+ \lesssim k_{s,FR}^+$, the breakdown of the Reynolds analogy is more mild. Although the data do not align with the Reynolds analogy curve, the predicted trend of a continual increase of $\Delta\Theta^+$ with k_s^+ is still preserved. However, in the fully rough regime, where $k_s^+ \gtrsim k_{s,FR}^+$, the breakdown becomes more pronounced, and $\Delta\Theta^+$ exhibits an entirely different behaviour with respect to k_s^+ compared with ΔU^+.

This breakdown of the analogy between heat and momentum transfer for rough walls has been documented exhaustively in the literature (e.g. Dipprey & Sabersky 1963; Owen & Thomson 1963; Brutsaert 1975; MacDonald *et al.* 2019). Conventionally, this breakdown is attributed to the introduction of pressure drag owing to bluff roughness elements, and the lack of any heat-transfer analogue to this mechanism (Owen & Thomson 1963). While heat transfer at a fluid–solid interface will occur solely through molecular conduction, momentum transfer (drag) may occur through the action of viscous stresses (the momentum analogue to conduction) or pressure drag, the latter of which will be dominant in the fully rough regime (MacDonald *et al.* 2019; Peeters & Sandham 2019). Consequently, the most drastic departures in the behaviour of momentum transfer (drag ΔU^+ or C_f) and heat transfer ($\Delta\Theta^+$ or C_h) is observed in the fully rough regime, as seen in figure 6(*a*,*c*). In the subsequent sections, we will elaborate on how this fully rough heat transfer can be modelled, motivated by observations of the flow locally.

3.4. *Exposed and sheltered flow*

In this section, we will provide a local view of the flow and heat-transfer behaviour in the vicinity of the roughness elements. Our primary motive will be to establish, based on observation, that the local flow (and heat transfer) can be idealised as a combination of two distinct behaviours: sheltered and exposed. In this context, the designation 'sheltered' pertains to regions of reversed flow characterised by diminished and uniformly distributed heat transfer. Conversely, the term 'exposed' signifies regions subjected to elevated shear, resulting in intensified heat-transfer patterns. These distinct behaviours will then later form the basis of a predictive model we propose in § 4. The notion of sheltered flow in particular is not new to the roughness literature and has been extensively covered, especially in the context of drag (e.g. Macdonald *et al.* 1998; Yang *et al.* 2016; Forooghi *et al.* 2018*b*). Conceptually, the idea of flow sheltering is that the presence of bluff roughness elements can cause flow separation to occur locally, modifying the drag response of any given rough surface (Yang *et al.* 2016). Some authors have anticipated that this flow-sheltering effect is likely to have physical significance in the context of heat transfer but have primarily based this intuition on global or mean measures of the heat transfer (Forooghi *et al.* 2018*b*; Peeters & Sandham 2019). Here, we will directly examine these local variations in the heat transfer q_w and their relation to the local flow behaviour. In figures 7(*a*)–7(*c*), we show ensemble-averaged visualisations of the streamwise velocity for our surfaces with $\Lambda = 0.09$–0.36 and for a fixed $k^+ \approx 11$. We identify sheltered regions based on the reversed-flow contour level, $\overline{u^+} \leq 0$ (white line). These sheltered regions form in
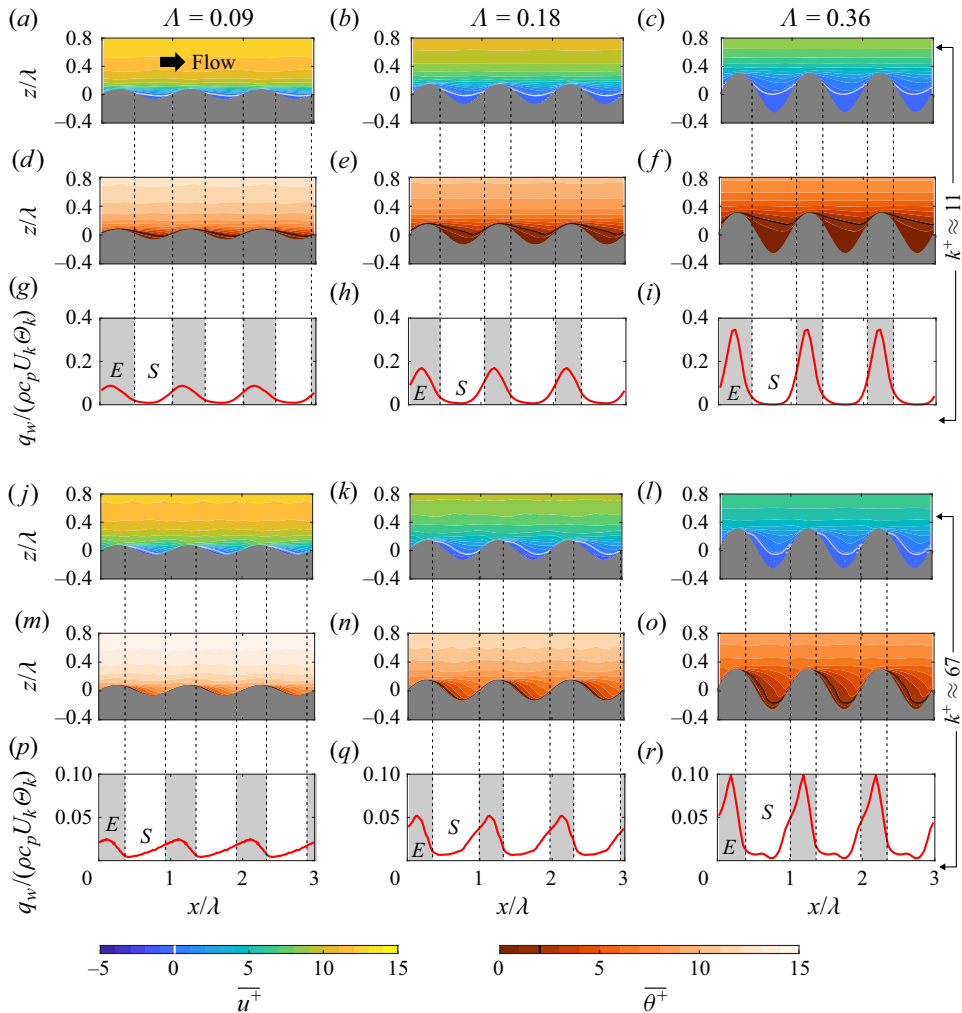
Figure 7. Time- and phase-averaged (*a*–*c*) streamwise velocity fields; (*d*–*f*) temperature fields; (*g*–*i*) and the local heat flux $q_w/(\rho c_p) = \alpha \partial\bar{\theta}/\partial n|_{wall}$ (non-dimensionalised by the crest velocity and temperature, U_k, Θ_k, respectively)for $k^+ \approx 11$ at varying Λ. The vertical grid lines track regions of sheltered flow ($\overline{u^+} < 0$, white lines), denoted by '*S*', and correlate with characteristically low q_w, while exposed (i.e. unsheltered) regions, denoted by '*E*', show spikes in q_w. The $\overline{\theta^+} = 2$ contours (black lines) roughly track regions of well-mixed temperature in the sheltered regions. (*j*–*r*) Same as (*a*–*i*) but for $k^+ \approx 67$.

leeward faces downstream from roughness elements and tend to grow in size with Λ. Unsheltered regions, which we generalise as being exposed regions, by contrast, tend to experience faster, high-shear flow. The influence of this flow on the temperature field can be seen in figures 7(*d*)–7(*f*), where we observe that sheltered regions tend to correlate with patches of well-mixed temperature (figure 7*d*–*f*, dark orange patches below the $\overline{\theta^+} = 2$ contours), which we highlight with temperature contours close to the wall value $\overline{\theta^+} = 2$ (black lines) and best seen for the highest solidity $\Lambda = 0.36$ (figure 7*f*). The well-mixed temperature regions correspond to weaker local heat transfer in sheltered regions (figure 7*g*–*i*), owing to the lower temperature gradients. Exposed regions, by contrast, tend to experience high-shear impinging flow, giving rise to sharper temperature

979 A22-20

gradients and thereby, higher heat transfer q_w. These exposed regions comprise the dominant contribution to the total heat transfer. The same trends appear as well at $k^+ \approx 67$ in the fully rough regime (figure 7j–r). These distinct sheltered and exposed heat-transfer signatures imply that we may understand the total heat transfer as comprising a dichotomy between two competing heat-transfer mechanisms in these sheltered and exposed regions. Their individual contributions to the total, integrated heat transfer is then a function of Λ as this parameter determines ultimately the fraction of sheltered and exposed flow (see changing proportion between shaded sheltered and unshaded exposed regions in figures 7(p)–7(r) with Λ). In light of this observation of different heat-transfer mechanisms observed in sheltered and exposed regions, we will develop a predictive model in the next section.

4. Predictive model

This section aims to develop a predictive model for heat transfer over rough walls as a function of k^+ and Λ. Having observed in § 3.4 that there is a meaningful difference in the local heat transfer between exposed and sheltered regions, we propose here a model that partitions the total heat transfer into separate heat-transfer laws for these regions. This is achieved by partitioning the physical definition of total wall heat flux (i.e. wall heat transfer per unit total plan area A_t) $\langle q_w \rangle / (\rho c_p) \equiv A_t^{-1} \int_w \alpha (\partial\theta/\partial n|_{wall}) \, \mathrm{d}A$ (Kays *et al.* 2005). Here, the subscript 'wall' denotes the 3-D rough surface. We decompose the wetted surface area, A_w, into an exposed area, A_e, and sheltered area, A_s, such that $A_w \equiv A_e + A_s$. Substituting this area partition into the physical definition of the heat flux and reorganising area fractions, e.g. $1/A_t = (A_e/A_w)(A_w/A_t)(1/A_e)$, we obtain

$$\frac{\langle q_w \rangle}{\rho c_p} \equiv \underbrace{\frac{A_e}{A_w} \frac{A_w}{A_t} \frac{1}{A_e} \int_e \alpha \left. \frac{\partial\theta}{\partial n}\right|_{wall} \mathrm{d}A}_{exposed} + \underbrace{\frac{A_s}{A_w} \frac{A_w}{A_t} \frac{1}{A_s} \int_s \alpha \left. \frac{\partial\theta}{\partial n}\right|_{wall} \mathrm{d}A}_{sheltered}, \tag{4.1}$$

$$C_{h,k} \equiv \frac{\langle q_w \rangle}{\rho c_p U_k \Theta_k} \equiv \frac{1}{U_k^+ \Theta_k^+} \equiv \frac{A_e}{A_w} \frac{A_w}{A_t} \underbrace{\frac{1}{A_e} \int_e \frac{\alpha \partial\theta/\partial n|_{wall}}{U_k \Theta_k} \mathrm{d}A}_{C_{h,e}}$$

$$+ \frac{A_s}{A_w} \frac{A_w}{A_t} \underbrace{\frac{1}{A_s} \int_s \frac{\alpha \partial\theta/\partial n|_{wall}}{U_k \Theta_k} \mathrm{d}A}_{C_{h,s}}$$

$$\equiv \frac{A_w}{A_t} \left[\left(\frac{A_e}{A_w}\right) C_{h,e} + \left(\frac{A_s}{A_w}\right) C_{h,s} \right]. \tag{4.2}$$

Here, (4.2) is a dimensionless form of (4.1), obtained by dividing (4.1) by $U_k \Theta_k$. The area fractions in (4.2) have been deliberately manipulated such that average heat-transfer coefficients in exposed and sheltered regions, $C_{h,e}$ and $C_{h,s}$, respectively, emerge. Weighted contributions between $C_{h,e}$ and $C_{h,s}$ based on exposed and sheltered area fractions, (A_e/A_w) and (A_s/A_w) will then contribute to the total rough-wall heat-transfer coefficient, $C_{h,k}$. These heat-transfer coefficients, $C_{h,k}$, $C_{h,e}$, $C_{h,s}$ are all defined on the crest velocity and temperature, U_k, Θ_k, respectively. The fraction A_w/A_t expresses the ratio of wetted to total plan area and is dependent on the roughness geometry only (a function of Λ for our present sinusoids), which may be treated as known. Note that $C_{h,k}$ can be

related to the g-function we introduced in (1.3b) by definition: $C_{h,k} \equiv \langle q_w \rangle / (\rho c_p U_k \Theta_k) \equiv g^{-1}(\Theta_{k_s}/\Theta_k)(U_\tau/U_k)$, where $\Theta_{k_s} \equiv \Theta(z - d = k_s)$ and $g \equiv \Theta_{k_s}^+$ (Dipprey & Sabersky 1963; Webb *et al.* 1971; Brutsaert 1975). One may pass between $C_{h,k}$ and g provided the ratios (Θ_{k_s}/Θ_k), $(U_\tau/U_k) \equiv (1/U_k^+)$ are known. These ratios are reported for our present cases in table 3 and both approach constant values in the fully rough regime dependent on Λ. Equations (4.1)–(4.2) are exact relations, but provide no predictive capability until models for the heat-transfer coefficients, $C_{h,e}$, $C_{h,s}$ and area fractions (A_e/A_w), (A_s/A_w) are prescribed. We will dedicate § 4.1 to pursuing a model representation for the exposed–sheltered area decomposition, such that (A_e/A_w), (A_s/A_w) may be determined, while § 4.2 will detail our heat-transfer models for $C_{h,e}$, $C_{h,s}$. All terms on the right-hand side of (4.2) will then be known and our final $C_{h,k} = f(k^+, \Lambda)$ model will be compared against DNS data in § 4.3.

4.1. *Sheltered–exposed area decomposition*

In this section, we present an analysis of techniques for estimating the exposed and sheltered regions, both through direct analysis of the DNS data and through the use of a ray-tracing model derived from the roughness geometry. Additionally, we propose a simplified fitting expression for predicting the area fractions (A_e/A_w and A_s/A_w), based on the ray-tracing model. First, we estimate the sheltered regions directly from the DNS by whether the time-averaged $u^+ = 0$ isosurface that lies above the roughness covers the underlying surface. If not, the flow is considered exposed. The red isosurface in figure 8(a) is at $\overline{u^+} = 0$ for $\Lambda = 0.18$ and $k^+ \approx 33$, showing the area covered within the recirculation region. The area partition produced from the isosurface is illustrated in the xy−plane in figure 8(d) where the sheltered and exposed regions are shown by the white and black contours respectively (labelled 'S' and 'E', respectively). A further possible method to estimate the sheltered and exposed regions is from the local, time-averaged viscous stresses $\tau_v/\rho \equiv \nu(\partial u/\partial n|_{wall})$. Here, we note that the local τ_v differs from the total wall shear stress, $\langle \tau_w \rangle$, from which the global friction velocity $U_\tau \equiv (\langle \tau_w \rangle/\rho)^{1/2}$ has been defined in § 1, as $\langle \tau_w \rangle$ encompasses both the viscous and pressure drag contributions for rough walls. From this τ_v method, the sheltered regions are determined as the area enclosed by the $\tau_v = 0$ contour (red line in figure 8b). The area partition produced from the former method in figure 8(d) and from the time-averaged contours of the $\tau_v = 0$ in figure 8(e) produce comparable results with no more than 7 % difference of the produced area partition for all cases.

The predictions of the exposed and sheltered regions in figures 8(a,d) and 8(b,e) require the flow fields. To enable prediction of the area fraction without need for computing flow fields, we obtained the exposed and sheltered regions directly from the roughness geometry. For this technique (called ray tracing), we assume that the sheltering extends as a straight line from the crest to the consecutive roughness element with an angle θ_s measured from the horizontal line, as previously proposed by Yang *et al.* (2016) and shown here in figure 8(c). For simplicity, the sheltering angle for the ray tracing, is assumed constant (i.e. independent of k^+ and Λ) at $\theta_s = 15°$, although θ_s obtained from DNS data using the $\overline{u^+} = 0$ isosurface method (figure 8a) varied in the range $\theta_s = 8°$–$15°$ over the three solidity cases and approached a constant value of $\theta_s \approx 10°$, $13°$ and $15°$ for $\Lambda = 0.09$, 0.18 and 0.36, respectively, in the fully rough regime. The estimation of θ_s through the $\overline{u^+} = 0$ isosurface can be exemplified, for instance, by figure 7(a). In this case, θ_s corresponds to the angle of a straight-line approximation fitted to the sheltering contour (white line). Angles in the vicinity of this range (i.e. $\theta_s \approx 15°$) are
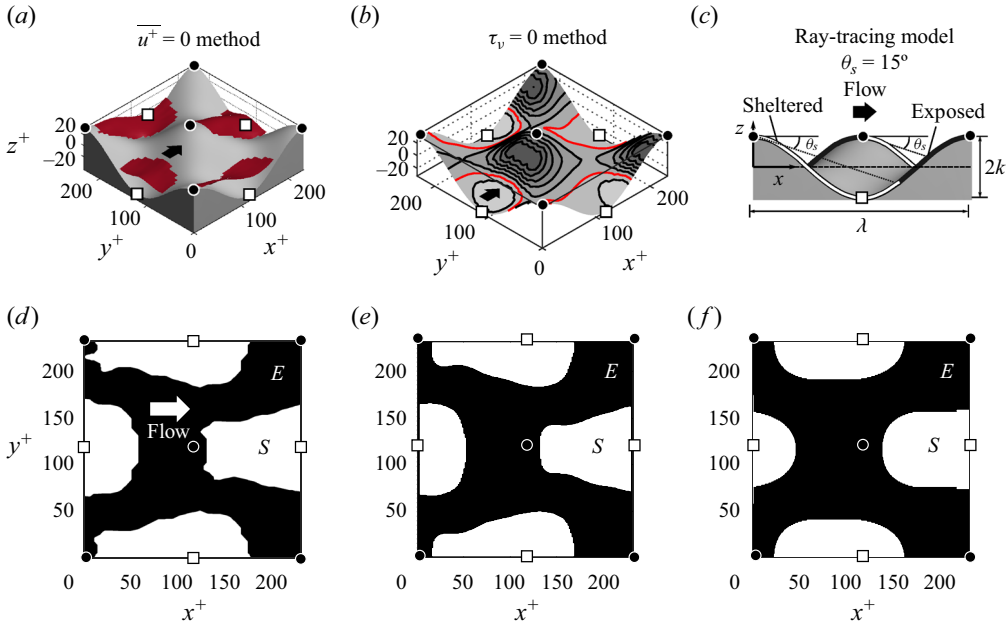
Figure 8. Methods employed for determining sheltered and exposed areas using the $k^+ = 33$ and $\Lambda = 0.18$ case as an example. Throughout, roughness peaks and valleys are marked by black circles and white squares, respectively. (*a*) Sheltered regions are determined by whether the $\overline{u^+} = 0$ isosurface (red) covers the underlying flow. If not, the flow is considered exposed. (*b*) Time-averaged contours of the viscous stress $\tau_\nu/\rho \equiv \nu \partial \bar{u}/\partial n|_{wall}$ (darker for increasing magnitude). Sheltered regions are determined as the area enclosed by the $\tau_\nu = 0$ contour (red line) and exposed otherwise. (*c*) The sheltering is modelled as a straight line starting from the crest and angled with sheltering angle (θ_s). The exposed and sheltered areas are shown with black and white lines in (*c*), respectively. Area partition produced from (*d*) the isosurface $\overline{u^+} = 0$; (*e*) the $\tau_\nu = 0$ isocontour and; (*f*) the sheltering model. Sheltered regions are shown by white filled contours (labelled '*S*') and exposed regions are shown in black (labelled '*E*').

typical of those found for separated flows (Raupach 1992; Prasad & Williamson 1997; Yang *et al.* 2016, 2022). Figure 8(*f*) shows that the area partition from the straight-line sheltering assumption with $\theta_s = 15°$ can provide a reasonable prediction of the area fractions compared with the other methods. Figure 9 shows the area fraction from the time-averaged contours of $\tau_\nu = 0$ and the ray tracing of the straight-line sheltering for the three solidity cases at fixed $k^+ \approx 33$. The validity of the straight sheltering assumption (as shown in figure 9*e*–*f*) for $\Lambda = 0.18$ and 0.36 is demonstrated by the good approximation of the area partition compared with figure 9(*b*,*c*). However, for the case of low solidity with $\Lambda = 0.09$, the straight-line sheltering assumption appears to underestimate the sheltered area (as illustrated in figure 9*d*) in contrast to the area partition in figure 9(*a*). This may be attributed to either the inaccurate estimation of θ_s for the low solidity, or the assumption of no lateral spreading, as will be discussed below.

The straight-line sheltering assumption clearly does not account for the lateral spreading that is evident in the flow field data (e.g. figure 9*a*–*c*). This lateral spreading could also be included into the current model following the same approach as Millward-Hopkins *et al.* (2011), who developed an empirical relation to relate the lateral spreading angle to the roughness height and width for uniform cube array roughness. However, the current technique appears to provide reasonable area fraction prediction with minimal assumptions.
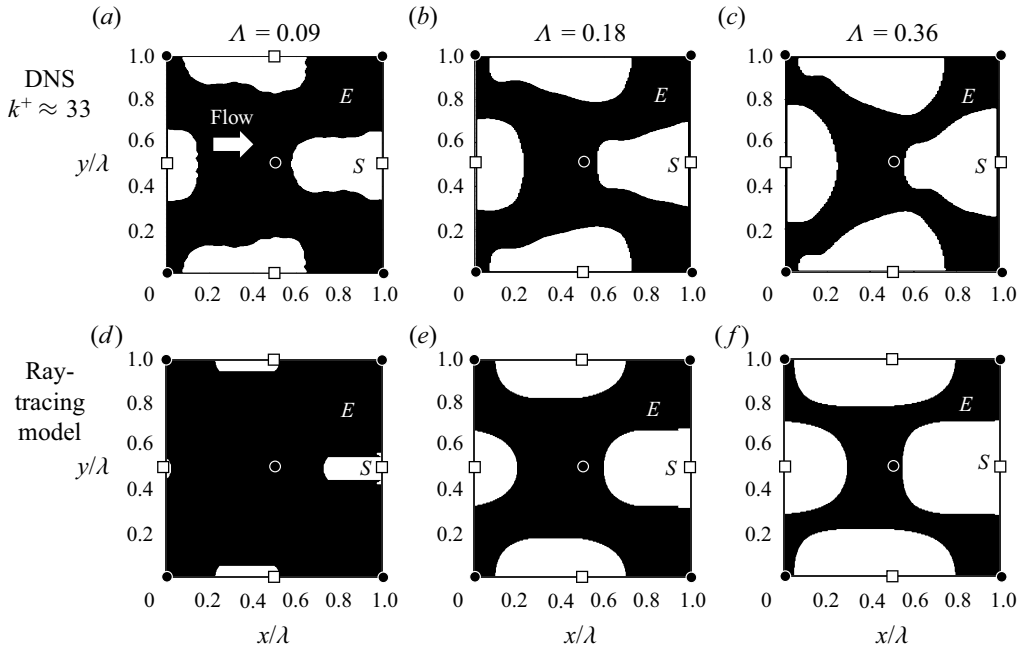
Figure 9. Comparison between sheltered–exposed area partitions at varying Λ for (a–c) the present DNS at $k^+ \approx 33$ computed obtained from the $\tau_v = 0$ partition and (d–f) the present model adopting a fixed sheltering angle, $\theta_s \approx 15°$. White patches correspond to the sheltered ('S') area, while black patches are for the exposed ('E') area. Black circles and white squares mark roughness peaks and valleys, respectively.

The previous results demonstrate that, while the ray-tracing technique is a reliable tool for predicting the area fraction of 3-D sinusoidal roughness, it lacks a closed-form analytical expression, which may make its implementation in a predictive model cumbersome. For our present 3-D sinusoids, the area ratio A_e/A_w from ray-tracing may instead be well approximated by the following empirical relation:

$$\frac{A_e}{A_w} = \min\left(1.0, \ 0.5\left(\frac{\tan(\theta_s)}{\Lambda}\right)^{1/2}\right), \tag{4.3}$$

where θ_s is the sheltering angle, as illustrated in figure 8(c) and assumed throughout to be $15°$. A limiting condition when all wetted areas are exposed $A_e = A_w$ is incorporated into (4.3). The sheltered area fraction will follow from $A_s/A_w \equiv 1 - A_e/A_w$. Figure 10 shows the good agreement of the area fraction expression (4.3) with the DNS data. The DNS data in figure 10 A_e/A_w are computed from the $\tau_v = 0$ contour method (figure 8b,e). Figure 10 also shows the ray-tracing representation (grey lines) of the exposed to wetted area ratio for validation of the fit (4.3). The comparison with our present DNS also validates one crucial simplification used in our area fraction expression of (4.3), namely, that this area fraction is independent of k^+, which appears to approximately hold true for larger k^+. Thus, hereafter in this section, the area fraction expression (4.3) will be used to determine (A_e/A_w and A_s/A_w).
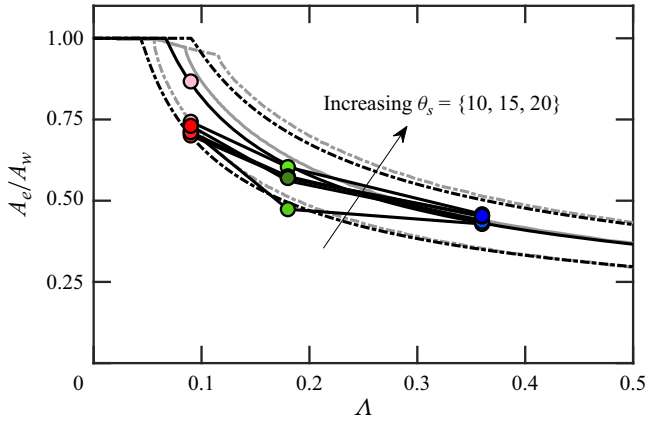
979 A22-24

Figure 10. Exposed wetted area fraction A_e/A_w. The markers show area fractions determined from the DNS, based on the $\tau_\nu = 0$ contour method, with the same marker styles as figure 6. These data are compared against the ray-tracing algorithm (grey lines) and the area ratio expression (4.3) (black lines) for varying choices of the sheltering angle θ_s, with a best fit of $\theta_s \approx 15°$.
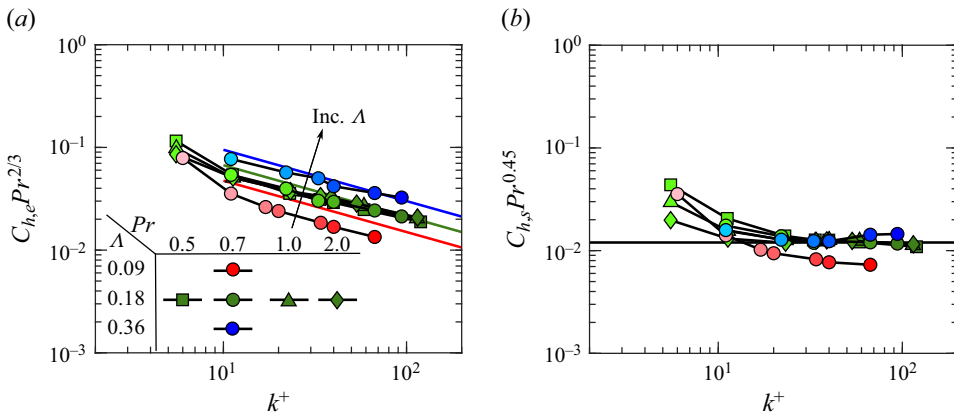

Figure 11. (*a*) The exposed heat-transfer coefficient $C_{h,e}$ for the present DNS (markers with lines). The marker styles are the same as in figure 6. Direct numerical simulations at fixed $\Lambda = 0.18$ for varying Pr from Zhong *et al.* (2023) have also been included. The exposed heat-transfer model $C_{h,e}Pr^{2/3} = 0.5(k^+)^{-1/2}\Lambda^{1/2}$ is shown by the coloured lines matching each solidity in the DNS. (*b*) Sheltered heat-transfer coefficient compensated by an empirical Prandtl number scaling $C_{h,s}Pr^{0.45}$. The present model approximates (4.5) this behaviour as both a $C_{h,s} \approx 0.012Pr^{-0.45}$ (horizontal black line) and zero.

4.2. *Sheltered–exposed heat-transfer models*

Here, we will provide details on the exposed and sheltered heat-transfer models for $C_{h,e}$, $C_{h,s}$ required in (4.2) for prediction. For the present DNS, $C_{h,e}$ and $C_{h,s}$ are computed using the exposed–sheltered decomposition obtained from the $\tau_\nu = 0$ contour method (e.g. figure 8*b*,*e*), consistent with figures 9 and 10. Figure 11 summarises the content we will present in this section. Namely, models for $C_{h,e} = f(k^+, \Lambda)$ and $C_{h,s} = f(k^+, \Lambda)$ and a comparison with the current DNS and that of Zhong *et al.* (2023) (markers).

To model the exposed heat transfer, we will adopt a Reynolds-analogy-type model, $C_{h,e} \propto (k^+)^{-1/2}\Lambda^{1/2}Pr^{-2/3}$. The model hinges on the phenomenological ideas of Owen & Thomson (1963) and Yaglom & Kader (1974), where they postulated that the local

viscous–conductive regions close to the roughness elements behave analogously to a flat-plate laminar boundary layer. The intuition is restricted to the fully rough regime (high-k^+) such that a scale separation between the roughness height and viscous scale emerges $k \gg \nu/U_\tau$. Owing to this scale separation, they envision the flow locally as having attached thermal and viscous boundary layers, developing over the roughness height k. The consequence in envisioning this phenomenology, as argued by Owen & Thomson (1963) and Yaglom & Kader (1974), is that we may then generalise the Reynolds-analogy prediction for heat transfer $C_{h,x} \propto Re_x^{-1/2}Pr^{-2/3}$ (Kays *et al.* 2005) to the case of a rough wall. Here, $Re_x \equiv xU_\infty/\nu$ is a Reynolds number based on the streamwise development length, x and free-stream velocity, U_∞, while $C_{h,x} \equiv q_{w,x}/(\rho c_p U_\infty \Theta_\infty)$ is the dimensionless heat transfer (Stanton number) defined on the free-stream temperature relative to the wall, Θ_∞. In generalising to a rough wall, Owen & Thomson (1963) and Yaglom & Kader (1974) set the streamwise fetch as $x \propto k$ and the velocity and temperature scales, $U_\infty \propto U_\tau \propto U_k$, $\Theta_\infty \propto \Theta_k$. Adopting these relations, this generalises $Re_x \equiv xU_\infty/\nu$ to the roughness Reynolds number $k^+ \equiv kU_\tau/\nu$ and the heat transfer $C_{h,x} \equiv q_{w,x}/(\rho c_p U_\infty \Theta_\infty)$ to a rough-wall heat-transfer coefficient, say, $C_{h,k}$, yielding the predictions: $C_{h,k} \propto (k^+)^{-1/2}Pr^{-2/3}$.

Our present work will adopt two additional modifications to the original form put forward by Owen & Thomson (1963) and Yaglom & Kader (1974), such that the prediction may be sensitised to the solidity, Λ. First, rather than take the Reynolds-analogy model to describe the total heat transfer, $C_{h,k}$, we instead only take it to describe the exposed heat transfer, $C_{h,e}$. The intuition underpinning this decision is based on the observations from figure 7, where we isolate that it is only in the windward, exposed regions where the flow remains attached and tends to experience high-shear flow, correlating to higher heat transfer. Consequently, we may expect ideas from a canonical wall-attached boundary-layer flow to be applicable in these regions. Notably, this behaviour is distinct when compared with sheltered regions which appear to follow a different heat-transfer scaling entirely. Second, rather than taking $x \propto k$ as the streamwise fetch, we instead take $x \propto \lambda$. The intuition underpinning this choice comes from recognising that x is understood as the wall-parallel development length of the boundary layer. Thus, rather than taking x to be analogous to the roughness height k in the case of a rough wall, the more appropriate analogue to take for x would be the local arc length along the roughness topography over which the local boundary layer may develop. In the interest of simplicity, we may approximate as the in-plane roughness length scale λ. Adopting these changes, the model changes from $C_{h,k} \propto (k^+)^{-1/2}Pr^{-2/3}$ to $C_{h,e} \propto (\lambda^+)^{-1/2}Pr^{-2/3}$, since $\lambda \propto k/\Lambda$ by definition

$$C_{h,e} = 0.5(k^+)^{-1/2}\Lambda^{1/2}Pr^{-2/3}, \tag{4.4}$$

where the 0.5 pre-factor is a tuning constant. As seen in figure 11(*a*), (4.4) is able to capture the scaling trends of our present DNS reasonably well, best seen for our high-Λ cases ($\gtrsim 0.18$). Although the model may appear to work well for transitionally rough values of k^+ (i.e. non-fully rough), this is not by design. Strictly speaking, our $C_{h,e}$ model is best applied to the fully rough regime, as the greater $k \gg \nu/U_\tau$ scale separation helps to ensure that the postulated phenomenology of a local laminar boundary layer is upheld. From figure 11(*a*), however, we see that our $C_{h,e}$ model still performs well in the transitionally rough regime at $k^+ \approx O(10)$. Over a smooth wall, the viscous sublayer (i.e. the local laminar boundary layer) has a characteristic thickness of $5\nu/U_\tau$ (Pope 2000). Consequently, moderate transitionally rough values of $k^+ \approx O(10)$ may not provide significant scale separation between the roughness size k and the boundary-layer thickness

$5\nu/U_\tau$. It is moreover expected that our model should fail if low-k^+ values are considered such that k is smaller than or of comparable size to $5\nu/U_\tau$. The roughness elements in this instance are submerged below or of comparable size to the viscous sublayer thickness (e.g. Luchini 1996). Consequently, this would invalidate the phenomenology of a local laminar boundary layer developing over the roughness topography which (4.4) relies upon, owing to insufficient scale separation between k and $5\nu/U_\tau$. To verify the validity of the Reynolds-analogy $Pr^{-2/3}$ scaling, we have also included in figure 11(*a*) data from the DNS of Zhong *et al.* (2023). The study considered an identical 3-D sinusoidal roughness with fixed $\Lambda = 0.18$, while varying k^+ and *Pr*. As evidenced by figure 11(*a*), the $Pr^{-2/3}$ scaling yields an excellent collapse for the exposed heat transfer, $C_{h,e}$, within the limited investigated range of $0.5 \lesssim Pr \lesssim 2.0$.

We now consider a model for the sheltered heat transfer, $C_{h,s}$. Figure 11(*b*) shows $C_{h,s}$ for the present DNS as well as the $\Lambda = 0.18$, varying *Pr* data from Zhong *et al.* (2023). Here, we observe a behaviour where $C_{h,s}$ is held approximately constant with k^+ in the fully rough regime (high-k^+), with a mild dependence on the constant value with respect to Λ as well as a dependency on *Pr*. A similar behaviour can be observed when examining the local variations in figure 7(*d–f*) or (*p–r*) where the heat transfer is held approximately uniform in sheltered regions. Of notable difference, however, is how the exposed heat transfer tends to provide the dominant contribution to the total when examining figure 7(*p–r*), but when taking integrated measures across the entire surface area (i.e. $C_{h,e}$ and $C_{h,s}$), the trends of figure 11(*a,b*) suggest both $C_{h,e}$ and $C_{h,s}$ will approach similar orders of magnitude for larger k^+. Slight qualitative differences will also be present in comparing the sheltered regions of figure 7 and the sheltered heat transfer $C_{h,s}$ in figure 11(*b*), as $C_{h,s}$ is computed based on sheltered regions from the $\tau_\nu = 0$ contour (figure 10*b,e*) whereas, in figure 7, sheltered regions are identified as reversed-flow regions ($\overline{u^+} = 0$). In light of these observations and in the interest of a model of maximal simplicity, we will test two separate models for the sheltered heat transfer

$$C_{h,s} = 0.012 Pr^{-0.45}, \quad C_{h,s} = 0. \tag{4.5a,b}$$

The first option $C_{h,s} = 0.0012 Pr^{-0.45}$ is an empirical fit to the medium–high solidity data (figure 11*b*, black line). The second option of $C_{h,s} = 0$ coincides with the physical assumption that the total heat transfer, $C_{h,k}$, may be predicted solely through the exposed contribution in (4.2) alone and is one of the simplest approximations one may have arrived at based on the q_w observations of figure 7(*p–r*). It is worth noting that this approximation may not align with the integrated sheltered heat transfer $C_{h,s}$ (figure 11*b*), as $C_{h,e}$ and $C_{h,s}$ can approach similar orders of magnitude at higher k^+. Despite this, we will still examine the case where $C_{h,s} = 0$ in order to assess its impact on the total rough-wall heat-transfer coefficient, $C_{h,k}$.

4.3. *Model comparison data*

In this section, we compare our present model with the $C_{h,k}$ measured from the DNS, having now given various expressions in (4.3), (4.4) and (4.5) as required in (4.2) for prediction. Figure 12 presents the comparison against our present DNS. Adopting the choice of $C_{h,s} = 0.012 Pr^{-0.45}$ (solid lines), our model captures the trend of the data reasonably well, best seen for the higher solidity cases. Worth noting too is the performance of the model prediction when neglecting any sheltered contribution, $C_{h,s} = 0$ (dashed lines). Here, we see that the dominant scaling behaviour of $C_{h,k}$ with respect to k^+ can still be maintained despite this, and does not suffer too harshly in performance
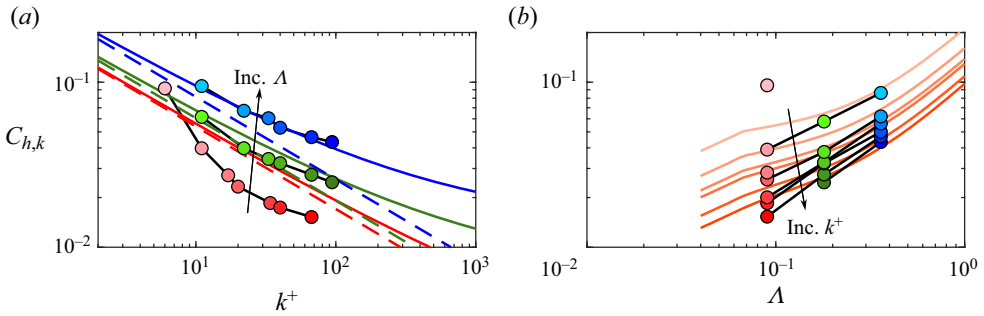
Figure 12. (*a*) The rough-wall heat-transfer coefficient $C_{h,k}$ for our present DNS (coloured markers) compared against our present model (coloured lines) from (4.2) using the various proposals of (4.3)–(4.5) and a fixed sheltering angle, $\theta_s \approx 15°$. The solid lines adopt a constant sheltered heat transfer $C_{h,s} = 0.012Pr^{-0.45}$ while the dashed lines neglect the sheltered heat-transfer contribution ($C_{h,s} = 0$). The solid lines adopt a constant sheltered heat transfer $C_{h,s} = 0.012Pr^{-0.45}$ while the dashed lines neglect the sheltered heat-transfer contribution ($C_{h,s} = 0$), resulting in less accurate predictions of $C_{h,k}$. (*b*) Value of $C_{h,k}$ plotted with respect to Λ (darker coloured lines correspond to increasing k^+). The black lines connect DNS data at matched values of k^+. Only model lines with constant $C_{h,s} = 0.012Pr^{-0.45}$ are shown for clarity.

for $k^+ \approx 30$–100. This result then showcases that one may obtain a good estimate for the total heat transfer, $C_{h,k}$, by solely considering contributions from exposed regions of the flow for this k^+ range. We emphasise the final point in particular regarding the k^+ range, because as seen in figure 12(*a*) the $C_{h,s} = 0.012Pr^{-0.45}$ and $C_{h,s} = 0$ choices eventually produce disparate asymptotic behaviours for $C_{h,k}$ for higher k^+, indicating that sheltered heat transfer may become prominent further into the fully rough regime.

A further comment can be made regarding the range of validity with respect to Λ of our present model. The model framework relies on a clear distinction between exposed and sheltered regions which for particular limits of Λ may be ill defined. For sparse–wavy regimes ($\Lambda \to 0$), smooth-wall conditions potentially absent of any flow separation will be approached (Raupach *et al.* 1991; MacDonald *et al.* 2016), which would invalidate the concept of sheltered flow. Although for our $\Lambda = 0.09$ case, flow separation can be observed locally (cf. figure 7*a*,*j*, $\overline{u^+} \le 0$), the differences in the sheltered and exposed heat-transfer magnitudes are not as pronounced compared with the higher solidity cases (compare figure 7*p* with *q*,*r*). Consequently, the distinction between sheltered and exposed behaviour is perhaps not as evident for our $\Lambda = 0.09$ case, which could explain why our present model is less successful for $\Lambda = 0.09$.

It is instructive to demonstrate that our framework for predicting the rough-wall heat-transfer coefficient, $C_{h,k}$, is also capable of handling different roughness topographies. Here, we have applied our framework to the experimental 2-D rib data of Webb *et al.* (1971). Owing to the different geometry, applying the ray-tracing exercise as was done for our present sinusoids in § 4.1 will yield different expressions for the exposed–sheltered area fractions, A_e/A_w, A_s/A_w required for prediction of $C_{h,k}$ from (4.2). These details have been left to Appendix B, and, identically to our present sinusoids, yield expressions solely determined by Λ and an assumed sheltering angle θ_s. Recall that the constant prefactors for the exposed and sheltered heat-transfer coefficient $C_{h,e} = 0.5(k^+)^{-1/2}\Lambda^{1/2}Pr^{-2/3}$, $C_{h,s} = 0.012Pr^{-0.45}$ and sheltering angle $\theta_s = 15°$ were obtained by tuning to our present DNS (figure 11), where the partitions for $C_{h,e}$ and $C_{h,s}$ were readily accessible. Presumably, these constants are likely dependent on the specific roughness topography and need to be tuned, but for the experimental data of Webb *et al.*
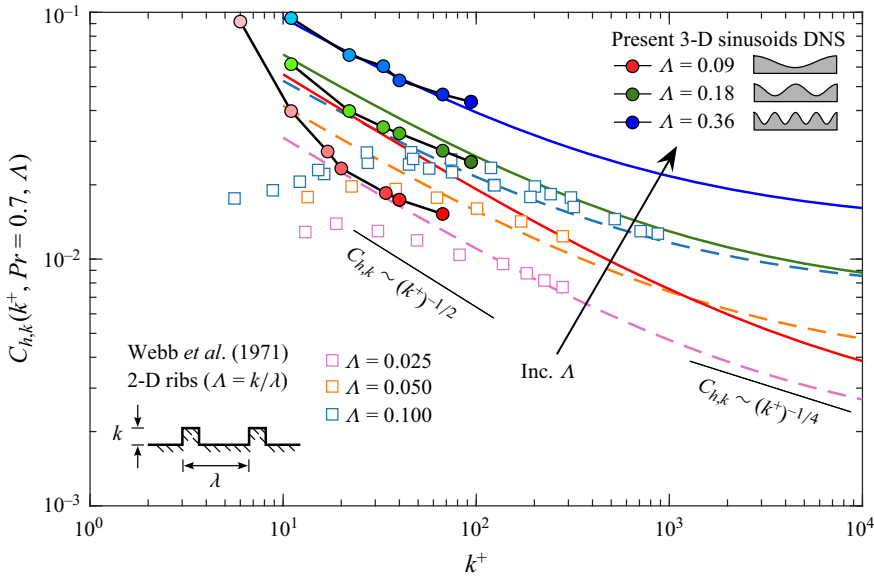
979 A22-28

Figure 13. The rough-wall heat-transfer coefficient $C_{h,k}$ at $Pr = 0.7$ for the present DNS (markers with lines) and the 2-D rib experiments of Webb *et al.* (1971) (square markers). The model predictions at each Λ (solid lines for present 3-D sinusoids, dashed lines for 2-D ribs) all employ the same model constants, $C_{h,e} = 0.5(k^+)^{-1/2} \Lambda^{1/2} Pr^{-2/3}$, $C_{h,s} = 0.012 Pr^{-0.45}$, and sheltering angle $\theta_s = 15°$. The area models employed for the 2-D ribs are given by (B1)–(B2).

(1971), only the total coefficient $C_{h,k}$ is available. Consequently, we make no attempt to tune these coefficients, instead keeping them the same as the ones used for our present sinusoids. In figure 13, we show a comparison between our present model and the $C_{h,k}$ of both our present DNS and data of Webb *et al.* (1971). Our model shows excellent agreement in capturing the fully rough (high-k^+) data of Webb *et al.* (1971), despite not having made any changes to the $C_{h,e}$, $C_{h,s}$ constant prefactors and sheltering angle, $\theta_s = 15°$. The trends of $C_{h,k}$ with respect to Λ are also well captured. These results then demonstrate that our sheltered–exposed framework has the potential to generalise well to arbitrary roughness geometries. It is worth mentioning that the current model yields accurate predictions for the 2-D rib data of Webb *et al.* (1971), even when low solidities of $\Lambda = 0.025$ are considered. This contrasts with the discrepancy noted between the model predictions and the DNS case of low solidity ($\Lambda = 0.09$) for the present 3-D sinusoids. This distinction might be attributed to the presence of sharp corners in the 2-D rib geometry, which forces the flow to separate and helps to ensure that there exist distinct sheltered and exposed regions: a key assumption of our present model.

Next, we discuss the effective scaling behaviour of our model $C_{h,k} \sim (k^+)^{-p}$, where the correct value to take for the exponent p has remained a topic of debate (e.g. Li *et al.* 2017, 2020; Chung *et al.* 2021; Zhong *et al.* 2023). Amongst theoretical proposals of note are the $p = 1/2$ Reynolds-analogy-type proposal of Owen & Thomson (1963), Yaglom & Kader (1974) and the $p = 1/4$ surface-renewal scaling of Brutsaert (1975). It has been argued that this scaling exponent may perhaps depend on the roughness topography (Li *et al.* 2020) and in some cases it has been hinted that this exponent varies with spatial location (Meinders, Hanjalic & Martinuzzi 1999; Nakamura, Igarashi & Tsutsui 2001; Li *et al.* 2016). This latter intuition is one that directly coincides with our proposed

model, where, namely, we have proposed that in exposed regions, $C_{h,e} \sim (k^+)^{-1/2}$ and for sheltered, $C_{h,s} \sim (k^+)^0$. Recall from (4.2) that the total heat-transfer coefficient follows from a weighted sum (based on area fractions dependent on Λ) between $C_{h,e}$ and $C_{h,s}$. In this sense, our $C_{h,k}$ model can be interpreted as a 'blending' function between a $C_{h,k} \sim (k^+)^{-1/2}$ and $C_{h,k} \sim (k^+)^0$ scaling behaviour, where the aggregated behaviour between these two scalings can potentially emerge as the surface-renewal scaling $C_{h,k} \sim (k^+)^{-1/4}$ depending on the particular value of Λ and k^+ (figure 13). Thus, in contrast to past rough-wall heat-transfer theories, our present model framework proposes that rough-wall heat transfer is determined not by any singular mechanism (e.g. Reynolds analogy or surface renewal) but rather by a blending of distinct behaviours, where presently we identify these distinct behaviours as a sheltered and exposed behaviour.

Finally, we end this section by highlighting that our rough-wall heat-transfer coefficient has been defined on crest values, $C_{h,k} \equiv 1/(U_k^+ \Theta_k^+)$. Although definitions based on crest values may be common in the roughness literature (e.g. Dipprey & Sabersky 1963; Webb *et al.* 1971; Macdonald *et al.* 1998), a more relevant quantity for practitioners to use in prediction may be an integrated or full-scale heat-transfer coefficient, e.g. the bulk Stanton number C_h. Therefore, in Appendix C we have provided comprehensive details on how our proposed $C_{h,k}$ model can be extended to enable full-scale prediction of the integrated heat transfer, C_h.

5. Conclusions

To further understand the influence of the frontal solidity, Λ and roughness Reynolds number, k^+, on global and local rough-wall heat transfer, we have conducted direct numerical simulations over a 3-D sinusoidal roughness. We considered three values of roughness density ($\Lambda = 0.09, 0.18$ and 0.36) and a range of roughness heights. With increasing roughness height, k^+, we observe a change of the heat-transfer regime with $\Delta\Theta^+$ approaching a plateau for $\Lambda = 0.09$ at $k^+ \gtrsim 33$ and for $\Lambda = 0.18$ at $k^+ \gtrsim 40$. For $\Lambda = 0.36$, both ΔU^+ and $\Delta\Theta^+$ continue to increase with k^+ up to $k^+ \approx 94$, although with signs that $\Delta\Theta^+$ approaches a plateau at $k^+ \approx 94$. These results suggested that the breakdown of the analogy between heat and momentum transfer is dependent on Λ and occurs at higher values of k_s^+ for larger values of Λ. The velocity ΔU^+ and temperature $\Delta\Theta^+$ roughness functions, at fixed $k^+ \approx 11$ in the transitionally rough regime, increase with Λ for $\Lambda < 0.18$ and then decrease for $\Lambda > 0.18$. But in the fully rough regime, ΔU^+ and $\Delta\Theta^+$ continue to increase with Λ up to the simulated limit of $\Lambda \approx 0.36$. The trends for ΔU^+ and $\Delta\Theta^+$ with Λ in the fully rough regime for the present fixed-skewness regular surfaces therefore running contrary to the typical transitionally rough behaviour observed whereby ΔU^+ and $\Delta\Theta^+$ present broad peaks between sparse and dense regimes.

Local examination of the heat transfer revealed that one can idealise the local behaviour as two distinct behaviours: exposed, where the heat transfer is characteristically higher; and sheltered, where the heat transfer is held approximately uniform. This intuition forms the basis of a predictive model we propose, where we have partitioned both the total heat transfer and total area into an exposed and sheltered contribution. The area partition model may be solely determined based on a prescribed sheltering angle, $\theta_s \approx 15°$ given a solidity, Λ, while for heat transfer, distinct scaling behaviours are pursued in exposed and sheltered regions. We find that the exposed heat transfer, $C_{h,e}$, may be modelled through a rough-wall generalisation of the Reynolds analogy, which presently, we adopt as a modification from the ideas of Owen & Thomson (1963) and Yaglom & Kader (1974): $C_{h,e} \propto (k^+)^{-1/2} \Lambda^{1/2} Pr^{-2/3}$. The current DNS suggests that the sheltered heat

transfer $C_{h,s}$ is independent of k^+ and approaches a constant value in the fully rough regime, independent of k^+. The model for rough-wall heat-transfer coefficient $C_{h,k}$ shows a good agreement with the DNS results for the high solidity cases and within the limited investigated range of Pr ($0.5 \lesssim Pr \lesssim 2.0$). However, for the low solidity cases, precisely $\Lambda = 0.09$, the model overestimates $C_{h,k}$ compared with the DNS results. We speculate that the model's failure at low solidity for our present sinusoids is likely due to the ambiguity in identifying distinct sheltered and exposed regions, as the key assumption of our model is that the local flow can be partitioned into these two regions. This speculation may be further supported when we consider the success of our present model when applied to the 2-D ribs of Webb *et al.* (1971) over a broad range of solidities $\Lambda = 0.025$–0.100. Unlike our present 3-D sinusoids, the sharp corners present in the 2-D rib geometry ensure the flow separates locally, thus providing a clear sheltered flow region, even in the sparse $\Lambda = 0.025$ regime. Moreover, this sheltered–exposed dichotomy failing at low solidity for the 3-D sinusoids can be discerned from the model's inability to capture the individual exposed and sheltered heat-transfer coefficients, $C_{h,e}$ and $C_{h,s}$, respectively (figure 11). Even if the correct exposed–sheltered area decomposition were used (e.g. figure 9*a–c*) as opposed to our ray-tracing model, this would not remedy the mismatch between our model's $C_{h,e}$, $C_{h,s}$ predictions and the low solidity data, as no explicit dependence on the area decomposition enters in the prediction of $C_{h,e}$, $C_{h,s}$ model (cf. (4.4), (4.5)). These findings indicate that the applicability of our present sheltered–exposed framework is limited for low solidity roughness topographies, where the sheltered and exposed regions are not clearly distinguished (absent any sharp corners). In the future, it will be necessary to establish a clear threshold or metric for identifying 'suitably' separated flows (on which the current modelling framework is predicated).

Declaration of interests. The authors report no conflict of interest.

Author ORCIDs.

- W. Abu Rowin https://orcid.org/0000-0002-5727-8519;
- K. Zhong https://orcid.org/0000-0002-2484-4115;
- T. Jelly https://orcid.org/0000-0001-5314-7768;
- N. Hutchins https://orcid.org/0000-0003-1599-002X;
- D. Chung https://orcid.org/0000-0003-3732-364X.

Appendix A. Validation against MacDonald *et al.* (2019)

In order to verify the accuracy and reliability of the current DNS algorithm, results from the previous work of MacDonald *et al.* (2019) were reproduced. In that work, turbulent forced convection over 3-D sinusoids with a frontal solidity of $\Lambda = 0.18$ was simulated from transitionally to fully rough conditions using DNS. Here, we compare our group M data against the results of MacDonald *et al.* (2019) for the friction Reynolds-number range $395 \lesssim Re_\tau \lesssim 1680$ at matched frontal solidity of $\Lambda = 0.18$ (see table 2 for details). There are three key differences between the present study and the past work by MacDonald *et al.* (2019). First, their study used a minimal channel domain with the roughness topography applied to both the top and bottom walls, whereas our work uses an open-channel
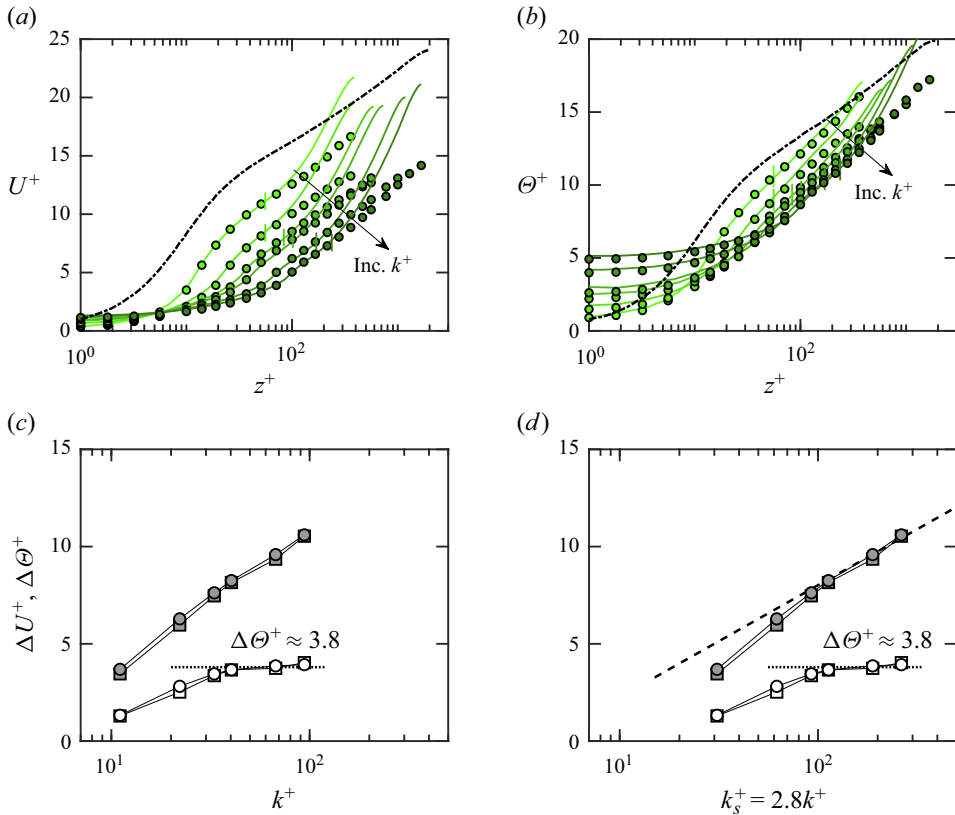
Figure 14. Validation against the past results of MacDonald *et al.* (2019) using current data from group M cases with the friction Reynolds-number range $395 \lesssim Re_\tau \lesssim 1680$ (see table 2). (*a*) Viscous-scaled streamwise mean velocity profiles, U^+, vs viscous-scaled wall-normal height, z^+. (*b*) Viscous-scaled mean temperature profiles, Θ^+, vs z^+. The darker shading refers to increasing k^+ as listed in table 2. In (*a,b*), MacDonald *et al.* (2019) data are shown with lines while the current group M data are shown with filled circles. The black dash-dotted line in (*a,b*) corresponds to the smooth-wall data of Bernardini *et al.* (2014) and Pirozzoli *et al.* (2016), respectively. The velocity roughness function, ΔU^+, (grey symbols) and temperature roughness function, $\Delta \Theta^+$, (white symbols) are shown vs (*c*) k^+ and (*d*) $k_s^+ = 2.8k^+$. Roughness functions of MacDonald *et al.* (2019) are shown with ($\square$) and group M are shown with ($\circ$). The black dashed line in (*d*) is the fully rough asymptote (1.2).

domain with roughness on the bottom wall only. Second, their study used a numerical algorithm with a body-conforming mesh to explicitly resolve the roughness geometry, an unstructured finite volume code named CDP (Mahesh, Constantinescu & Moin 2004), whereas our work uses an IBM based on volume of fluid interpolation. Third, as was previously mentioned, the spanwise domain width in their study was at least a factor of three narrower than any of the cases considered here. Despite these differences, the inner-scaled streamwise mean velocity and mean temperature profiles of the current work and the study by MacDonald *et al.* (2019) show excellent levels of agreement in the near-wall region, and, as shown in figure 14(*a,b*), are practically indistinguishable up to the wall-normal critical height, $z_c^+ = 0.4L_y^+$. On the other hand, considerable disagreement between the two data sets is observed for wall-normal heights greater than $z_c^+ > 0.4L_y^+$, which occurs due to the differing spanwise domain widths. Specifically, the wider spanwise domains used here result in so-called 'healthy' turbulence (Flores & Jiménez 2010) penetrating deeper into the outer layer, extending above the wall-normal critical

979 A22-32

(*a*) No mutual sheltering (tan $\theta_s \geq \Lambda$) (*b*) Mutual sheltering (tan $\theta_s < \Lambda$)

$$\frac{A_s}{A_w} = \frac{\Lambda(1 + \cot\theta_s)}{2\Lambda + 1} \qquad\qquad \frac{A_s}{A_w} = \frac{2\Lambda + 1 - \tan\theta_s}{2\Lambda + 1}$$
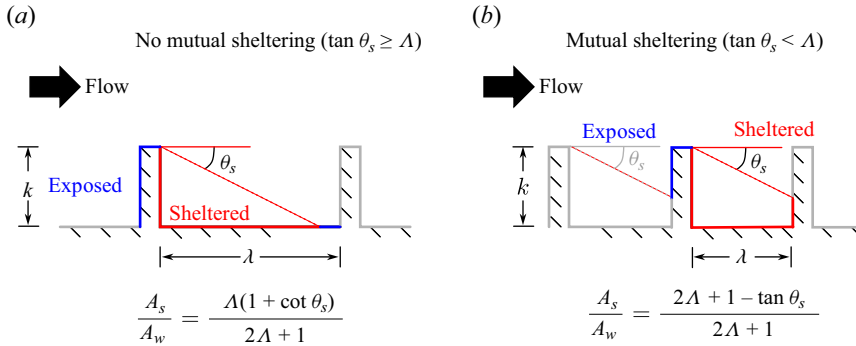
Figure 15. Schematic illustration of ray tracing applied to 2-D rib geometry. The framework is parameterised by the frontal solidity $\Lambda = k/\lambda$ and a tuning parameter in the sheltering angle θ_s. Two situations are demarcated: (*a*) no mutual sheltering and (*b*) mutual sheltering based on a critical sheltering angle condition tan $\theta_s = \Lambda$.

height of the minimal channel set-up adopted by MacDonald *et al.* (2019). However, since the outer layer of a minimal channel (or a minimal open channel) is inherently unphysical, differences in this region are inconsequential and do not affect the reliability of the mean velocity and temperature profiles in the near-wall region. The velocity roughness function, $\Delta U^+ = U_s^+(z) - U^+(z)$, and temperature difference function, $\Delta\Theta^+ = \Theta_s^+(z) - \Theta^+(z)$, are also compared against the past work of MacDonald *et al.* (2019) in figure 14(*c,d*). The values of $U_s^+(z)$ were taken from the smooth-wall turbulent channel flow data of Bernardini *et al.* (2014) at a friction Reynolds number of $Re_\tau \approx 2021$. Likewise, the values of $\Theta_s^+(z)$ were taken from the smooth-wall turbulent channel flow data of Pirozzoli *et al.* (2016) at matched flow conditions. In this comparison, ΔU^+ and $\Delta\Theta^+$ are computed at $z = 0.2h$, which is always less than z_c for the current data and the data of MacDonald *et al.* (2019). This method of computing ΔU^+ and $\Delta\Theta^+$ is different from that used in § 3.3. This approach results in small difference in ΔU^+ and $\Delta\Theta^+$ reported in MacDonald *et al.* (2019) as they used their simulated smooth data corresponding to each rough case for U_s^+ and Θ_s^+, respectively. In figure 14(*c*), an excellent level of agreement between the two data sets is observed. For both simulations, ΔU^+ increases with k^+, while $\Delta\Theta^+$ reaches a constant (≈ 3.8) at $k^+ \gtrsim 33$. Figure 14(*d*) shows ΔU^+ and $\Delta\Theta^+$ against the equivalent sand-grain roughness, $k_s \approx 2.8k$. The factor 2.8 is obtained from collapsing ΔU^+ with the fully rough asymptote (1.2). This factor is smaller than that reported in MacDonald *et al.* (2019) of $k_s/k \approx 4.1$, taken from Chan *et al.* (2015) presumably due to the different approach used here to estimate the roughness functions. The $k_s \approx 2.8k$ result also differs from the $k_s \approx 2.7k$ result we report in § 3 for $\Lambda = 0.18$ as this appendix does not consider any virtual origin influences (unlike in § 3).

Appendix B. Analytical ray-tracing model for 2-D ribs

This appendix details the ray-tracing methodology applied to the 2-D rib geometry studied in Webb *et al.* (1971), such that expressions for the area fractions A_e/A_w, A_s/A_w required in our model for the heat-transfer coefficient $C_{h,k}$ in (4.2) can be obtained. A schematic of the 2-D rib geometries is provided in figure 15 and the latter are characterised by a rib height k and spacing Λ with frontal solidity $\Lambda = k/\lambda$. In the following, we also assume that the ribs are of negligible thickness, such that the wetted-to-total area ratio is simply
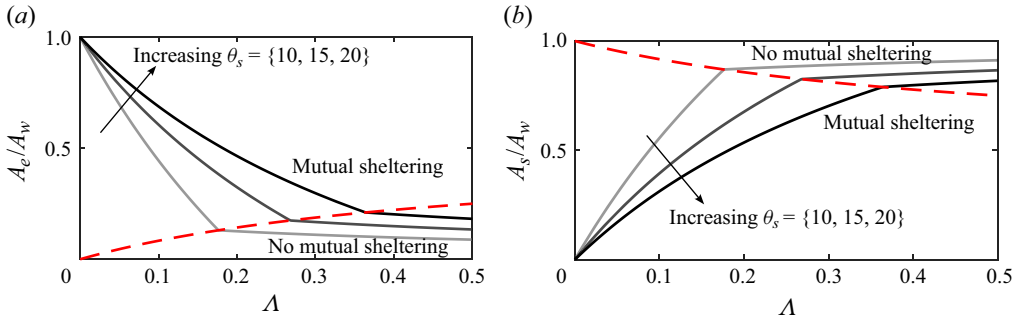
$$A_w/A_t = 2\Lambda + 1. \tag{B1}$$

Figure 16. (*a*) Exposed and (*b*) sheltered area fraction models obtained from simple ray tracing of 2-D ribs. The dashed red line, $\tan\theta_s = \Lambda$ demarcates the limit where mutual sheltering begins.

To model the exposed and sheltered area partition, a straight-line sheltering at an angle θ_s from the horizontal and from the rib peaks is assumed, consistent with our ray tracing for 3-D sinusoids in § 4.1. Two instances are isolated: one where the spacing between adjacent ribs is large such that no mutual sheltering occurs (figure 15*a*) and instances where mutual sheltering occurs (figure 15*b*) for closely packed ribs. It is a matter of trigonometry to show that these two instances can be demarcated by a critical sheltering angle, $\tan\theta_{s,crit} = \Lambda$ where for $\theta_s < \theta_{s,crit}$, mutual sheltering will occur. With reference to figure 15, the sheltered area fraction for these two instances are

$$
\frac{A_s}{A_w} = \begin{cases} \dfrac{\Lambda(1 + \cot\theta_s)}{2\Lambda + 1}, & \text{for } \tan\theta_s \geq \Lambda \quad \text{(no mutual sheltering),} \\[2ex] \dfrac{2\Lambda + 1 - \tan\theta_s}{2\Lambda + 1}, & \text{for } \tan\theta_s < \Lambda \quad \text{(mutual sheltering),} \end{cases} \tag{B2}
$$

where again we have neglected the thickness of the ribs. The exposed area fraction follows simply from $A_e/A_w = 1 - A_s/A_w$. Sample curves for this area model at varying sheltering angles θ_s are plotted in figure 16. Note that for the $\Lambda = 0.025$–0.100 range covered in the study of Webb *et al.* (1971), this will fall exclusively into the mutual sheltering range for the $\theta_s = 10°$–$20°$ range.

Appendix C. Full-scale prediction

The purpose of this appendix will be to demonstrate how our model for the rough-wall heat-transfer coefficient $C_{h,k}(k^+, \Lambda) \equiv 1/(U_k^+ \Theta_k^+)$ may be used for full-scale prediction of the outer-scale heat-transfer coefficient in the Stanton number, $C_h \equiv \langle q_w \rangle/(\rho c_p U_h \Theta_h) \equiv 1/(U_h^+ \Theta_h^+)$. This Stanton number is defined on the channel centreline velocity and temperature relative to the wall, U_h^+, and Θ_h^+ respectively. A global skin-friction coefficient, $C_f \equiv \langle \tau_w \rangle/(0.5\rho U_h^2) \equiv 2/(U_h^+)^2$ is also defined. These quantities will depend on a bulk Reynolds number, $Re \equiv 2hU_h/\nu$, a blockage ratio, k/h, and the solidity Λ. To link the rough-wall heat-transfer coefficient defined on the crest velocity and temperature, U_k^+ and Θ_k^+ to C_f, C_h, we assume logarithmic profiles

$$
U^+ = (1/\kappa)\log(z/k) + U_{k,log}^+, \tag{C1}
$$

$$
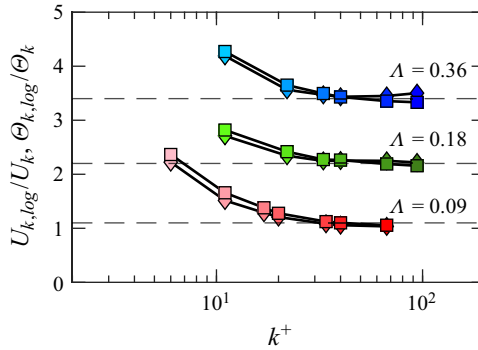\Theta^+ = (1/\kappa_h)\log(z/k) + \Theta_{k,log}^+, \tag{C2}
$$

Figure 17. Ratio of the crest velocity (diamond markers) and temperature (square markers) extrapolated from the log region, $U_{k,log}^+$, $\Theta_{k,log}^+$, to the measured crest values U_k^+, Θ_k^+. The data are staggered upwards by $+1$ and $+2$ for $\Lambda = 0.18$ and 0.36, respectively. In the fully rough regime, the ratios plateau to 1.1, 1.2 and 1.4 for $\Lambda = 0.09, 0.18, 0.36$.

then evaluate the expressions at the channel centreline $z = h$ to obtain U_h^+, Θ_h^+. For simplicity, we have neglected the virtual origin d and also any wake contributions. Note that, by neglecting d, this will introduce some discrepancies to the C_f, C_h values we report in table 3 which are obtained as extrapolations of the log region taking d into account. Here, there is a distinction made between the familiar crest velocity and temperature, U_k, Θ_k and $U_{k,log}$, $\Theta_{k,log}$, which are extrapolations of the log region to the crest location $z = k$. Formally, these can be defined in terms of k_s/k by combining (C1)–(C2) with $U^+ = (1/\kappa) \log(k_s^+) + C_N$, $\Theta^+ = (1/\kappa_h) \log(k_s^+) + g$ to obtain $U_{k,log}^+ = C_N - (1/\kappa) \log(k_s/k)$, $\Theta_{k,log}^+ = g - (1/\kappa_h) \log(k_s/k)$. In general, $U_k^+ \neq U_{k,log}^+$, $\Theta_k^+ \neq \Theta_{k,log}^+$ since we expect the crest location to lie within the roughness sublayer where the flow is inhomogeneous, where we would not expect the flow to follow the logarithmic profile. Many authors typically neglect this distinction (e.g. Macdonald *et al.* 1998; Millward-Hopkins *et al.* 2011; Yang *et al.* 2016), since the scaling behaviours of the crest values U_k^+ and Θ_k^+ can be considered interchangeable with $U_{k,log}^+$, $\Theta_{k,log}^+$. We show this in figure 17, where the ratios $U_{k,log}/U_k$, $\Theta_{k,log}/\Theta_k$ approach constant values dependent on Λ. For $\Lambda = 0.09, 0.18, 0.36$, we have close-to-unity ratios of $U_{k,log}/U_k \approx \Theta_{k,log}/\Theta_k \approx 1.1, 1.2, 1.4$ respectively, with an empirical fit of $U_{k,log}/U_k \approx \Theta_{k,log}/\Theta_k \approx 1.65\Lambda^{0.17}$. That is, a mild dependence on Λ. These ratios enable us to pass from U_k^+, Θ_k^+ which $C_{h,k}$ is defined on to $U_{k,log}^+$, $\Theta_{k,log}^+$. Although this means one would require knowledge of the ratios in figure 17, we will demonstrate later that if we ignore this distinction (i.e. assume $U_{k,log} = U_k$, $\Theta_{k,log} = \Theta_k$), this will not significantly alter the trends of our model for full-scale prediction. Note that we have attempted (not shown here for brevity) to predict $\Delta\Theta^+$ by equating (C2) with (1.3a). When the estimated $\Delta\Theta^+$ is compared against $\Delta\Theta^+$ from DNS of figure 6(d), our model captures the observed trends of increasing $\Delta\Theta^+$ with Λ for $\Lambda \gtrsim 0.18$ provided accurate U_k^+ and $(\Theta_k^+/\Theta_{k,log}^+)$ shown in figure 17 are also known. However, the model's performance falls short in capturing the trend of increasing $\Delta\Theta^+$ with increasing k^+ for a fixed $\Lambda = 0.36$, as depicted in figure 6(b). This suggests that the current sheltered-exposed heat transfer modelling framework has the potential to predict $\Delta\Theta^+$ more accurately with the incorporation of models designed to estimate log intercepts, as demonstrated in figure 17, and heat-transfer coefficients designed for low solidity cases

We obtain C_f, C_h by evaluating (C1)–(C2) at the centreline, $z = h$

$$\sqrt{2/C_f} \equiv U_h^+ = (1/\kappa) \log(h/k) + U_{k,log}^+, \tag{C3}$$

$$\sqrt{C_f/2}/C_h \equiv \Theta_h^+ = (1/\kappa_h) \log(h/k) + \Theta_{k,log}^+. \tag{C4}$$

At this stage, we will define a 'log-corrected' rough-wall heat-transfer coefficient, $C_{h,k,log} \equiv 1/(U_{k,log}^+ \Theta_{k,log}^+) \equiv (U_k/U_{k,log})(\Theta_k/\Theta_{k,log})C_{h,k} \propto C_{h,k}$, such that one may pass from $C_{h,k,log}$ to $C_{h,k}$ using the prefactors reported in figure 17. By combining (C3)–(C4) to eliminate the $\log(h/k)$ term and recognising $\Theta_{k,log}^+ \equiv 1/(C_{h,k,log}U_{k,log}^+)$, we may obtain an explicit expression for C_h

$$C_h = \frac{C_f/2}{(\kappa/\kappa_h)(1 - \sqrt{C_f/2}U_{k,log}^+) + \sqrt{C_f/2}C_{h,k,log}^{-1}/U_{k,log}^+}. \tag{C5}$$

To compute C_h (and C_f) for varying Re and Λ, we require a drag model in the form of an expression for $U_{k,log}^+$. As the focus of our present work is not modelling drag, here, we will adopt a fit to our present DNS, $U_k^+ \approx 2.4\Lambda^{-0.43}$. This then enables C_f to be computed explicitly as a function of only k/h and Λ, independent of Re from (C3) once passing from U_k^+ to $U_{k,log}^+$ from the pre-factors of figure 17. This independence of C_f with respect to Re is a known feature of drag in the fully rough regime (Flack & Schultz 2010). With C_f, $U_{k,log}^+$ and $C_{h,k,log} \propto C_{h,k}(k^+, \Lambda)$ known, we may then compute C_h. Note that by definition, $k^+ \equiv 0.5Re(k/h)Re\sqrt{C_f/2}$ so that the k^+ dependency of $C_{h,k}$ may be passed to k/h and Re.

For model constants, we adopt $\kappa = 0.4$, $\kappa_h = 0.47$ and the best-fit parameters for our $C_{h,k}$ model, $C_{h,e} = 0.5(k^+)^{-1/2}\Lambda^{1/2}Pr^{-2/3}$, $C_{h,s} = 0.012Pr^{-0.45}$ and $\theta_s = 15°$. We may also compute smooth-wall curves for $C_f/2 \equiv 1/(U_h^+)^2$, $C_h \equiv 1/(U_h^+\Theta_h^+)$ from (1.1) and (1.3a) with $d^+ = 0$, $\Delta U^+ = \Delta \Theta^+ = 0$

$$\sqrt{2/C_f} \equiv U_h^+ = (1/\kappa) \log(0.5Re/U_h^+) + A \tag{C6}$$

$$\sqrt{C_f/2}/C_h \equiv \Theta_h^+ = (1/\kappa_h) \log(0.5Re/U_h^+) + A_h, \tag{C7}$$

where $A \approx 5.0$ and $A_h(Pr = 0.7) \approx 3.2$. Equation (C6) has the explicit solution $\sqrt{2/C_f} = (1/\kappa)\mathcal{W}[0.5\kappa Re\exp(A\kappa - 1)]$ where $\mathcal{W}$ is the product logarithm function (MacDonald *et al.* 2019). The full set of model curves are shown in figure 18. Here, we show data for a fixed $h/k = 18$ (figure 18a,b), which correspond only to our medium ($\Lambda = 0.18$) and high ($\Lambda = 0.36$) cases for $k^+ \geq 22$, and $h/k = 36$ (figure 18c,d) for $\Lambda = 0.09$, $k^+ \gtrsim 11$. The reason for this h/k separation is because our present DNS adopted choices of both $h/k = 18$ and $h/k = 36$ depending on Λ (cf. table 2). Despite the h/k values differing amongst choices in Λ of our DNS, it is possible to extrapolate the values of C_f, C_h from our DNS from one value of h/k to another through the following method, to enable a fixed h/k comparison across all Λ we consider. First, we adopt (C3)–(C4) and recognise that the log intercepts, $U_{k,log}^+$, $\Theta_{k,log}^+$ do not change with sufficiently large h/k. Then, taking (C3) as an example, we may evaluate the equation at two different choices of h/k and combine the equations to eliminate $U_{k,log}^+$. Supposing we wanted to extrapolate from $h/k = 36$ to $h/k = 18$, this exercise will yield us an explicit equation for $C_{f,18}$ where the subscript 18 denotes the value of C_f for $h/k = 18$ as desired: $\sqrt{2/C_{f,18}} = (1/\kappa) \log(18/36) + \sqrt{2/C_{f,36}}$ (the subscript 36 denotes the C_f value for $h/k = 36$). A similar method follows for (C4) to obtain an extrapolation of C_h. Our present model
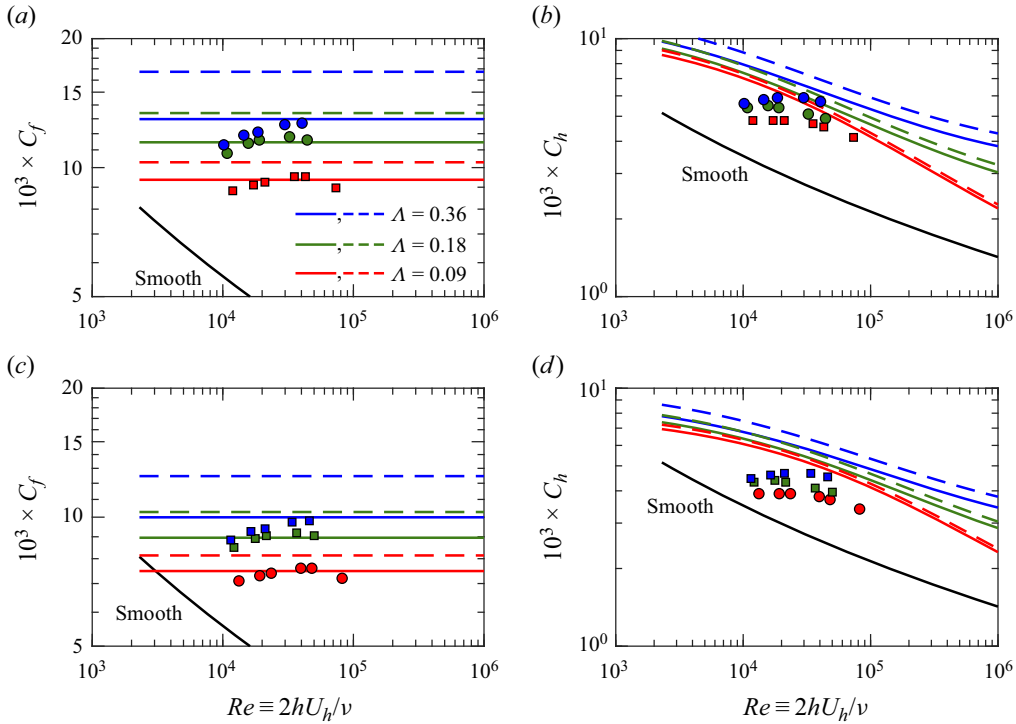
Figure 18. (*a*) The global skin-friction coefficient $C_f \equiv 2/(U_h^+)^2$; (*b*) Stanton number $C_h \equiv 1/(U_h^+ \Theta_h^+)$ at varying solidity Λ and fixed $h/k = 18$. The solid coloured lines are computed from our model equations (C3)–(C5), while the black lines are smooth-wall curves computed from (C6)–(C7). The coloured dashed lines correspond to our present model taking the ratios of figure 17 to be fixed at unity, $U_{k,log}/U_k = \Theta_{k,log}/\Theta_k = 1.0$. The markers are our present DNS, with values of C_f and C_h reported in table 3. Square markers indicate DNS data that have been extrapolated from a different value of h/k to the designated h/k of the panel (see body text for details), while circle markers indicate unextrapolated data as reported in table 3. (*c,d*) Same as (*a,b*) but for $h/k = 36$.

is compared against the present DNS data, where the square markers show data that have undergone this h/k extrapolation and circle markers show the unextrapolated, original data (i.e. no h/k extrapolation needed). Recall that in minimal channels, the flow is unphysical above a critical height $z_c = 0.4L_y < h$. Thus, in order to circumvent this and obtain the centreline measures U_h^+, Θ_h^+, required for C_f, C_h, we have simply extrapolated the logarithmic regions of our profiles to the centreline, then taken U_h^+, Θ_h^+ to be the values at the centreline, neglecting wake contributions. The values of C_f, C_h for the present DNS data are included in table 3. As seen in figure 18, the trends with respect to Λ are captured reasonably well by our present model. For a fixed h/k, the curves of increasing Λ may also be interpreted as a k_s/h effect: $k_s/h = (k/h)(k_s/k) \approx (h/k)(6.2\Lambda^{0.55})$ so that k_s/h is an increasing function of Λ. Our model curves of figure 18 are then consistent with the known increasing behaviour of C_f and C_h with respect to k_s/h (Webb *et al.* 1971; Chung *et al.* 2021). It is worth noting that a limitation of using our model for full-scale prediction is the requirement for knowledge of the pre-factors $U_{k,log}/U_k$ and $\Theta_{k,log}/\Theta_k$, such as those reported in figure 17, to convert from $U_{k,log}$ to U_k and $\Theta_{k,log}$ to Θ_k. The dashed lines of figure 18 present the model if this distinction were ignored, i.e. assuming $U_{k,log} = U_k$,

979 A22-37

$\Theta_{k,log} = \Theta_k$ such that $C_{h,k,log} = C_{h,k}$. Both drag (C_f) and heat transfer (C_h) are sensitive to this change but nevertheless, the primary trends with respect to Λ are still retained.

REFERENCES

ABDERRAHAMAN-ELENA, N., FAIRHALL, C. & GARCÍA-MAYORAL, R. 2019 Modulation of near-wall turbulence in the transitionally rough regime. *J. Fluid Mech.* **865**, 1042–1071.

ALCÁNTARA-ÁVILA, F., HOYAS, S. & PÉREZ-QUILES, M.J. 2021 Direct numerical simulation of thermal channel flow for. *J. Fluid Mech.* **916**, A29.

BERNARDINI, M., PIROZZOLI, S. & ORLANDI, P. 2014 Velocity statistics in turbulent channel flow up to. *J. Fluid Mech.* **742**, 171–191.

BRUTSAERT, W. 1975 A theory for local evaporation (or heat transfer) from rough and smooth surfaces at ground level. *Water Resour. Res.* **11** (4), 543–550.

BUSSE, A., THAKKAR, M. & SANDHAM, N. 2017 Reynolds-number dependence of the near-wall flow over irregular rough surfaces. *J. Fluid Mech.* **810**, 196–224.

CHAMBERLAIN, A.C. 1968 Transport of gases to and from surfaces with bluff and wave-like roughness elements. *Q. J. R. Meteorol. Soc.* **94** (401), 318–332.

CHAN, L., MACDONALD, M., CHUNG, D., HUTCHINS, N. & OOI, A. 2015 A systematic investigation of roughness height and wavelength in turbulent pipe flow in the transitionally rough regime. *J. Fluid Mech.* **771**, 743–777.

CHAN, L., MACDONALD, M., CHUNG, D., HUTCHINS, N. & OOI, A. 2018 Secondary motion in turbulent pipe flow with three-dimensional roughness. *J. Fluid Mech.* **854**, 5–33.

CHILTON, T.H. & COLBURN, A.P. 1934 Mass transfer (absorption) coefficients prediction from data on heat transfer and fluid friction. *Ind. Engng Chem.* **26** (11), 1183–1187.

CHUNG, D., CHAN, L., MACDONALD, M., HUTCHINS, N. & OOI, A. 2015 A fast direct numerical simulation method for characterising hydraulic roughness. *J. Fluid Mech.* **773**, 418–431.

CHUNG, D., HUTCHINS, N., SCHULTZ, M. & FLACK, K. 2021 Predicting the drag of rough surfaces. *Annu. Rev. Fluid Mech.* **53**, 439–471.

CLAUSER, F.H. 1954 Turbulent boundary layers in adverse pressure gradients. *J. Aeronaut. Sci* **21** (2), 91–108.

COLEBROOK, C. & WHITE, C. 1937 Experiments with fluid friction in roughened pipes. *Proc. R. Soc. Lond.* A **161** (906), 367–381.

DIPPREY, D. & SABERSKY, R. 1963 Heat and momentum transfer in smooth and rough tubes at various Prandtl numbers. *Intl J. Heat Mass Transfer* **6** (5), 329–353.

DIRLING, J.R. 1973 A method for computing roughwall heat transfer rates on reentry nosetips. In *8th Thermophysics Conference*, p. 763.

FACKRELL, J.E. 1984 Parameters characterising dispersion in the near wake of buildings. *J. Wind Engng Ind. Aerodyn.* **16** (1), 97–118.

FLACK, K.A. & SCHULTZ, M.P. 2010 Review of hydraulic roughness scales in the fully rough regime. *Trans. ASME J. Fluids Engng* **132** (4), 041203.

FLORES, O. & JIMÉNEZ, J. 2010 Hierarchy of minimal flow units in the logarithmic layer. *Phys. Fluids* **22** (7), 071704.

FOROOGHI, P., MAGAGNATO, F. & FROHNAPFEL, B. 2018a Reynolds analogy in turbulent flows over rough walls – a DNS investigation. In *International Journal of Heat Mass Transfer Conference Digital Library*. Begel House.

FOROOGHI, P., STRIPF, M. & FROHNAPFEL, B. 2018b A systematic study of turbulent heat transfer over rough walls. *Intl J. Heat Mass Transfer* **127**, 1157–1168.

FOROOGHI, P., STROH, A., SCHLATTER, P. & FROHNAPFEL, B. 2018c Direct numerical simulation of flow over dissimilar, randomly distributed roughness elements: a systematic study on the effect of surface morphology on turbulence. *Phys. Rev. Fluids* **3** (4), 044605.

GRAY, W.G. & LEE, P.C.Y. 1977 On the theorems for local volume averaging of multiphase systems. *Intl J. Multiphase Flow* **3** (4), 333–340.

HAMA, F.R. 1954 Boundary-layer characteristics for smooth and rough surfaces. *Trans. Soc. Nav. Archit. Mar. Engrs* **62**, 333–358.

HOYAS, S., OBERLACK, M., ALCÁNTARA-ÁVILA, F., KRAHEBERGER, S.V. & LAUX, J. 2022 Wall turbulence at high friction Reynolds numbers. *Phys. Rev. Fluids* **7** (1), 014602.

IBRAHIM, J., GÓMEZ-DE SEGURA, G., CHUNG, D. & GARCÍA-MAYORAL, R. 2021 The smooth-wall-like behaviour of turbulence over drag-altering surfaces: a unifying virtual-origin framework. *J. Fluid Mech.* **915**.

JACKSON, P.S. 1981 On the displacement height in the logarithmic velocity profile. *J. Fluid Mech.* **111**, 15–25.

JELLY, T.O., CHIN, R.C., ILLINGWORTH, S.J., MONTY, J.P., MARUSIC, I. & OOI, A.S.H. 2020 A direct comparison of pulsatile and non-pulsatile rough-wall turbulent pipe flow. *J. Fluid Mech.* **895**, R3.

JI, Y., YUAN, K. & CHUNG, J. 2006 Numerical simulation of wall roughness on gaseous flow and heat transfer in a microchannel. *Intl J. Heat Mass Transfer* **49** (7–8), 1329–1339.

JIMÉNEZ, J. 2004 Turbulent flows over rough walls. *Annu. Rev. Fluid Mech.* **36**, 173–196.

KADER, B. 1981 Temperature and concentration profiles in fully turbulent boundary layers. *Intl J. Heat Mass Transfer* **24** (9), 1541–1544.

KASAGI, N., TOMITA, Y. & KURODA, A. 1992 Direct numerical simulation of passive scalar field in a turbulent channel flow. *Trans. ASME J. Heat Transfer* **114** (3), 598–606.

KAYS, W.M., CRAWFORD, M.E. & WEIGAND, B. 2005 *Convective Heat and Mass Transfer*. 4th edn. McGraw-Hill.

KIM, J. & MOIN, P. 1989 Transport of passive scalars in a turbulent channel flow. In *Turbulent Shear Flows 6: Selected Papers from the Sixth International Symposium on Turbulent Shear Flows, Université Paul Sabatier, Toulouse, France, September 7–9, 1987*, pp. 85–96. Springer.

KUWATA, Y. 2021 Direct numerical simulation of turbulent heat transfer on the Reynolds analogy over irregular rough surfaces. *Intl J. Heat Fluid Flow* **92**, 108859.

KUWATA, Y. & NAGURA, R. 2020 Direct numerical simulation on the effects of surface slope and skewness on rough-wall turbulence. *Phys. Fluids* **32** (10), 105113.

LEE, M. & MOSER, R.D. 2015 Direct numerical simulation of turbulent channel flow up to $Re_\tau \approx 5200$. *J. Fluid Mech.* **774**, 395–415.

LEONARD, B.P. 1979 A stable and accurate convective modelling procedure based on quadratic upstream interpolation. *Comput. Meth. Appl. Mech. Engng* **19** (1), 59–98.

LEONARDI, S., ORLANDI, P., DJENIDI, L. & ANTONIA, R. 2015 Heat transfer in a turbulent channel flow with square bars or circular rods on one wall. *J. Fluid Mech.* **776**, 512.

LI, D., RIGDEN, A., SALVUCCI, G. & LIU, H. 2017 Reconciling the Reynolds number dependence of scalar roughness length and laminar resistance. *Geophys. Res. Lett.* **44** (7), 3193–3200.

LI, Q., BOU-ZEID, E., ANDERSON, W., GRIMMOND, S. & HULTMARK, M. 2016 Quality and reliability of LES of convective scalar transfer at high Reynolds numbers. *Intl J. Heat Mass Transfer* **102**, 959–970.

LI, Q., BOU-ZEID, E., GRIMMOND, S., ZILITINKEVICH, S. & KATUL, G. 2020 Revisiting the relation between momentum and scalar roughness lengths of urban surfaces. *Q. J. R. Meteorol. Soc.* **146** (732), 3144–3164.

LIGRANI, P.M., OLIVEIRA, M.M. & BLASKOVICH, T. 2003 Comparison of heat transfer augmentation techniques. *AIAA J.* **41** (3), 337–362.

LUCHINI, P. 1996 Reducing the turbulent skin friction. In *Computational Methods in Applied Sciences 1996, Proceedings of the 3rd ECCOMAS CFD Conference*, pp. 465–470. Wiley.

LUCHINI, P. & QUADRIO, M. 2022 Wall turbulence and turbulent drag reduction. In *50+ Years of AIMETA: A Journey Through Theoretical and Applied Mechanics in Italy*, pp. 349–364. Springer.

MA, G., XU, C., SUNG, H. & HUANG, W. 2020 Scaling of rough-wall turbulence by the roughness height and steepness. *J. Fluid Mech.* **900**, R7.

MACDONALD, M., CHAN, L., CHUNG, D., HUTCHINS, N. & OOI, A. 2016 Turbulent flow over transitionally rough surfaces with varying roughness densities. *J. Fluid Mech.* **804**, 130–161.

MACDONALD, M., CHUNG, D., HUTCHINS, N., CHAN, L., OOI, A. & GARCÍA-MAYORAL, R. 2017 The minimal-span channel for rough-wall turbulent flows. *J. Fluid Mech.* **816**, 5–42.

MACDONALD, M., HUTCHINS, N. & CHUNG, D. 2019 Roughness effects in turbulent forced convection. *J. Fluid Mech.* **861**, 138–162.

MACDONALD, R.W., GRIFFITHS, R.F. & HALL, D.J. 1998 An improved method for the estimation of surface roughness of obstacle arrays. *Atmos. Environ.* **32** (11), 1857–1864.

MAHESH, K., CONSTANTINESCU, G. & MOIN, P. 2004 A numerical method for large-eddy simulation in complex geometries. *J. Comput. Phys.* **197** (1), 215–240.

MARUSIC, I. & MONTY, J.P. 2019 Attached eddy model of wall turbulence. *Annu. Rev. Fluid Mech.* **51**, 49–74.

MEINDERS, E.R., HANJALIC, K. & MARTINUZZI, R.J. 1999 Experimental study of the local convection heat transfer from a wall-mounted cube in turbulent channel flow. *Trans. ASME J. Heat Transfer* **121** (3), 564–573.

MILLWARD-HOPKINS, J., TOMLIN, A., MA, L., INGHAM, D. & POURKASHANIAN, M. 2011 Estimating aerodynamic parameters of urban-like surfaces with heterogeneous building heights. *Boundary-Layer Meteorol.* **141** (3), 443–465.

MIYAKE, Y., TSUJIMOTO, K. & NAKAJI, M. 2001 Direct numerical simulation of rough-wall heat transfer in a turbulent channel flow. *Intl J. Heat Fluid Flow* **22** (3), 237–244.

NAKAMURA, H., IGARASHI, T. & TSUTSUI, T. 2001 Local heat transfer around a wall-mounted cube in the turbulent boundary layer. *Intl J. Heat Mass Transfer* **44** (18), 3385–3395.

NAPOLI, E., ARMENIO, V. & DE MARCHIS, M. 2008 The effect of the slope of irregularly distributed roughness elements on turbulent wall-bounded flows. *J. Fluid Mech.* **613**, 385–394.

NICKELS, T.B. 2004 Inner scaling for wall-bounded flows subject to large pressure gradients. *J. Fluid Mech.* **521**, 217.

NIKURADSE, J. 1933 Laws of flow in rough pipes. In *VDI Forschungsheft* (Engl. transl. 1950 in *NACA Tech. Rep.* 1292).

OWEN, P. & THOMSON, W. 1963 Heat transfer across rough surfaces. *J. Fluid Mech.* **15** (3), 321–334.

PEETERS, J. & SANDHAM, N. 2019 Turbulent heat transfer in channels with irregular roughness. *Intl J. Heat Mass Transfer* **138**, 454–467.

PEROT, J.B. 1993 An analysis of the fractional step method. *J. Comput. Phys.* **108** (1), 51–58.

PERRY, A.E. & JOUBERT, P.N. 1963 Rough-wall boundary layers in adverse pressure gradients. *J. Fluid Mech.* **17** (2), 193–211.

PERRY, A.E., SCHOFIELD, W.H. & JOUBERT, P.N. 1969 Rough wall turbulent boundary layers. *J. Fluid Mech.* **37** (2), 383–413.

PIROZZOLI, S. 2023 An explicit representation for mean profiles and fluxes in forced passive scalar convection. *J. Fluid Mech.* **968**, R1.

PIROZZOLI, S., BERNARDINI, M. & ORLANDI, P. 2016 Passive scalars in turbulent channel flow at high Reynolds number. *J. Fluid Mech.* **788**, 614–639.

PIROZZOLI, S., ROMERO, J., FATICA, M., VERZICCO, R. & ORLANDI, P. 2021 One-point statistics for turbulent pipe flow up to. *J. Fluid Mech.* **926**, A28.

PLACIDI, M. & GANAPATHISUBRAMANI, B. 2015 Effects of frontal and plan solidities on aerodynamic parameters and the roughness sublayer in turbulent boundary layers. *J. Fluid Mech.* **782**, 541–566.

POPE, S.B. 2000 *Turbulent Flows*. Cambridge University Press.

PRASAD, A. & WILLIAMSON, C.H.K. 1997 Three-dimensional effects in turbulent bluff-body wakes. *J. Fluid Mech.* **343**, 235–265.

RAUPACH, M.R. 1992 Drag and drag partition on rough surfaces. *Boundary-Layer Meteorol.* **60** (4), 375–395.

RAUPACH, M.R., ANTONIA, R.A. & RAJAGOPALAN, S. 1991 Rough-wall turbulent boundary layers. *Appl. Mech. Rev.* **44** (1), 1–25.

VAN RIJ, J., BELNAP, B. & LIGRANI, P. 2002 Analysis and experiments on three-dimensional, irregular surface roughness. *Trans. ASME J. Fluids Engng* **124** (3), 671–677.

ROUHI, A., CHUNG, D. & HUTCHINS, N. 2019 Direct numerical simulation of open-channel flow over smooth-to-rough and rough-to-smooth step changes. *J. Fluid Mech.* **866**, 450–486.

ROUHI, A., LOHSE, D., MARUSIC, I., SUN, C. & CHUNG, D. 2021 Coriolis effect on centrifugal buoyancy-driven convection in a thin cylindrical shell. *J. Fluid Mech.* **910**, A32.

SCHLICHTING, H. 1936 Experimentelle untersuchungen zum rauhigkeitsproblem. *Inge-Arch* **7** (1), 1–34 (Engl. transl. 1937. Experimental investigation of the problem of surface roughness. NACA TM 823).

SHARMA, A. & GARCÍA-MAYORAL, R. 2020 Scaling and dynamics of turbulence over sparse canopies. *J. Fluid Mech.* **888**, A1.

SHERIFF, N. & GUMLEY, P. 1966 Heat-transfer and friction properties of surfaces with discrete roughnesses. *Intl J. Heat Mass Transfer* **9** (12), 1297–1320.

SIMPSON, R. 1973 A generalized correlation of roughness density effects on the turbulent boundary layer. *AIAA J.* **11** (2), 242–244.

SPALART, P., MOSER, R. & ROGERS, M. 1991 Spectral methods for the Navier–Stokes equations with one infinite and two periodic directions. *J. Comput. Phys.* **96** (2), 297–324.

VERSTAPPEN, R. & VELDMAN, A. 2003 Symmetry-preserving discretization of turbulent flow. *J. Comput. Phys.* **187** (1), 343–368.

WAIGH, D.R. & KIND, R.J. 1998 Improved aerodynamic characterization of regular three-dimensional roughness. *AIAA J.* **36** (6), 1117–1119.

WEBB, R., ECKERT, E. & GOLDSTEIN, R. 1971 Heat transfer and friction in tubes with repeated-rib roughness. *Intl J. Heat Mass Transfer* **14** (4), 601–617.

YAGLOM, A. 1979 Similarity laws for constant-pressure and pressure-gradient turbulent wall flows. *Annu. Rev. Fluid Mech* **11** (1), 505–540.

YAGLOM, A. & KADER, B. 1974 Heat and mass transfer between a rough wall and turbulent fluid flow at high Reynolds and Péclet numbers. *J. Fluid Mech.* **62** (3), 601–623.

YANG, J., STROH, A., CHUNG, D. & FOROOGHI, P. 2022 Direct numerical simulation-based characterization of pseudo-random roughness in minimal channels. *J. Fluid Mech.* **941**, A47.

YANG, J., VELANDIA, J., BANSMER, S., STROH, A. & FOROOGHI, P. 2023 A comparison of hydrodynamic and thermal properties of artificially generated against realistic rough surfaces. *Intl J. Heat Fluid Flow* **99**, 109093.

YANG, X.I.A., SADIQUE, J., MITTAL, R. & MENEVEAU, C. 2016 Exponential roughness layer and analytical model for turbulent boundary layer flow over rectangular-prism roughness elements. *J. Fluid Mech.* **789**, 127–165.

YUAN, J. & PIOMELLI, U. 2014 Estimation and prediction of the roughness function on realistic surfaces. *J. Turbul.* **15** (6), 350–365.

ZHONG, K., HUTCHINS, N. & CHUNG, D. 2023 Heat-transfer scaling at moderate Prandtl numbers in the fully rough regime. *J. Fluid Mech.* **959**, A8.